Fluvial reworking eliminates small craters, but does not meaningfully bias the Mars interbedded-crater record

Andrew J. Moodie[1,2], Timothy A. Goudge[2,3]

[1]Department of Geography, Texas A&M University
[2]Department of Earth and Planetary Sciences, Jackson School of Geosciences, The University of Texas at Austin
[3]Center for Planetary Systems Habitability, The University of Texas at Austin

Key Points:

- We simulated coeval river-delta and crater production, and quantified crater preservation in resulting fluvial-deltaic stratigraphy
- Our findings indicate smaller craters are more often removed by fluvial reworking than larger craters
- More smaller craters are produced than rivers can remove, bolstering some interpretations of atmospheric paleo-pressure

THIS IS PREPRINT OF A RESEARCH ARTICLE SUBMITTED TO *Journal of Geophysical Research: Planets* ON 08/09/24. IT HAS NOT COMPLETED PEER REVIEW, AND HAS NOT BEEN ACCEPTED FOR PUBLICATION.

Corresponding author: Andrew J. Moodie, amoodie@tamu.edu

Abstract

Interpreting the structures, morphology, and chemistry of the exposed stratigraphic record on Mars is complicated by ancient surface processes that have variably removed parts of the record. Previous research has used the lack of smaller craters (≤50 m diameter) interbedded with fluvial deposits to constrain atmospheric pressure when rivers were active on Mars; the notion being that higher atmospheric pressure would have prevented smaller craters from forming. We hypothesize that contemporaneous channel lateral migration and avulsion could have reworked sedimentary deposits and eliminated craters from the stratigraphic record, thereby undermining atmospheric paleo-pressure interpretations. To test this hypothesis, we simulated coeval river-delta development and crater production, and quantified crater preservation in resulting stratigraphy. We document widespread crater rim degradation (∼67% of craters ≤50 m are at least partially eroded), and observe a marked increase in preservation with increasing crater diameter. That is to say, fluvial reworking preferentially removes smaller craters from the stratigraphic record. However, synthetic crater-diameter distributions incorporating fluvial reworking effects do not reproduce observations on Mars, because many smaller craters generated remain preserved in the simulated stratigraphy. We find that, although river channels are sometimes in the right place to eliminate crater deposits from the stratigraphic record, production of smaller craters outpaces fluvial reworking under all modeled circumstances, and that a higher pressure ancient atmosphere is necessary to reproduce observations (i.e., consistent with existing interpretations of interbedded crater records). Our findings therefore bolster studies that assert fluvial reworking is not a primary control on smaller interbedded crater counts on Mars.

Plain Language Summary

Higher atmospheric pressure causes small impactors to break up before reaching the ground. So, researchers have used the lack of small craters observed from a specific time interval on Mars to infer what the atmospheric pressure was during that time interval. This has been particularly useful for early Mars, when water was thought to have been more abundant, implying the need for a thicker atmosphere. We hypothesized that another process, rivers migrating across the landscape, could preferentially remove small craters from the observable record, and had misled researchers into thinking the lack of craters was due to high atmospheric pressure on ancient Mars. We tested our hypothesis with numerical modeling, and found that while migrating rivers can remove craters from the record, this process cannot remove enough craters to explain the complete lack of small craters on Mars.

1 Introduction

Decades of research have leveraged the sedimentary structures, morphology, and chemistry of the exposed stratigraphic record on Mars to understand the evolution of the planet's ancient surface and atmosphere (e.g., Cabrol et al., 1999; Malin & Edgett, 2000; J. Grotzinger et al., 2005; Milliken et al., 2010; J. P. Grotzinger et al., 2012-09; Cardenas et al., 2017; Goudge et al., 2018; Bishop et al., 2018; Day et al., 2019; Cardenas & Lamb, 2022; Vasavada, 2022). Of particular interest, is the formation timing of alluvial and lacustrine features on Mars, because these features likely demarcate the extent and duration of past hydrological activity that could have enabled life on the planet's surface (e.g., Bhattacharya, 2005). Without any direct sample dating as of the time of writing, absolute temporal constraints on formation of these features are determined by measured crater size-frequency distributions (CSFDs) that are paired with expected crater production rate models (i.e., crater counting; Hartmann, 1966; Hartmann & Neukum, 2001; Ivanov, 2001; Fassett, 2016). Interpreting crater records, and in particular those records from a planet with active sedimentary surface processes, is complicated by the interplay of ancient and modern surface processes that create, eliminate, and expose stratigraphic features (Jerolmack & Sadler, 2007; Kim et al., 2014; Cardenas et al., 2022). For example, it is well known that modern surface processes can readily degrade smaller craters ($\lesssim$50 m) to the point the crater is unrecognizable (e.g., Hartmann, 1971; Fassett, 2016; Williams et al., 2018), and therefore bias the observed crater record. There remains considerable uncertainty in how and under what circumstances the Mars crater record is biased by surface processes (Williams et al., 2018), and what the impact of this bias is on sedimentary feature age estimates (M. Golombek et al., 2010).

The lack of smaller craters ($\lesssim$50 m) embedded in the Mars stratigraphic record that is now exposed at the surface, has been used to constrain atmospheric paleo-pressure (e.g., Figure 1a; Kite et al., 2014; Warren et al., 2019). These studies determine atmospheric pressure from crater sizes by assuming a relationship between atmospheric pressure and the smallest size of impactors that can reach the planet surface before complete ablation (e.g., higher atmospheric pressure raises the lower limit of possible crater size; Popova et al., 2003; Williams et al., 2014). The additional assumption that atmospheric ablation is the only significant process impacting crater size distributions, enables an inversion from the measured CSFDs to atmospheric paleo-pressure, yielding an upper-bound pressure, in essence, based on the *lack* of smaller craters. Kite et al. (2014) isolated craters interbedded with fluvial deposits and that therefore formed when Mars rivers were active, and determined that the Mars atmosphere would have been less than $\sim$1.9 bar approximately 3.5 Ga. In another study using a similar approach, Warren et al. (2019) found that Mars paleo-pressure was approximately 1.5 and 1.9 bar at 3.8 and 4 Ga, respectively (or oscillated around these values; Warren et al., 2019).

Atmospheric paleo-pressure interpretations are especially sensitive to identification of smaller craters ($\lesssim$50 m). Prior studies have examined preferential destruction of smaller craters due to wind-blown erosion (Öpik, 1966; Hartmann & Neukum, 2001), diffusive down-slope transport driven by subsequent impacts (Ross, 1968; Soderblom, 1970; A. Howard, 2004; Minton et al., 2015), and flattening by seismic-shaking (Schultz & Gault, 1975; Richardson et al., 2004, 2005), as well as covering by lava flows (Neukum & Horn, 1976; Hiesinger et al., 2002; Michael, 2013), and obliteration during formation of new craters (i.e., saturation; Woronow, 1977, 1978; M. R. Smith et al., 2008; Richardson, 2009; Minton et al., 2015). Other studies have discussed the potential for erosion by fluvial processes to remove smaller craters (Irwin et al., 2013; Matsubara et al., 2018), but this has not been examined in the context of craters that could become interbedded in a fluvial sedimentary deposit (e.g., those craters in Kite et al., 2014). The potential impact of smaller crater removal on paleo-pressure interpretations has not been rigorously evaluated.

River and delta activity is spatially and temporally heterogeneous, due to the movement of channels across the landscape over time (Schumm, 1985; Straub et al., 2009). This channel movement causes local fluctuations in deposition and erosion that create a stratigraphic record rife with gaps and bias in recorded time (Sadler, 1981; Hajek & Straub, 2017; Straub et al., 2020). For example, individual channel bends translate across the landscape eroding deposited material (e.g., Schumm, 1985), and leaving behind characteristic lateral accretion deposits, that are commensurate in height to the channel depth (e.g., Figure 1b; Edwards & Eri, 1983; Bridge & Mackey, 1992). At larger space and time scales, channels regularly relocate across the floodplain via avulsion, wherein flow is steered across the landscape surface by topography and a new channel pathway is developed (e.g., Frazier, 1967; Wells & Dorr, 1987; N. D. Smith et al., 1989; Hajek & Edmonds, 2014).

As a result of these channel movements, fluvial reworking of stratigraphy is scaled to a first order by channel depth and channel mobility (Leeder, 1978; Ganti et al., 2011; Straub & Esposito,

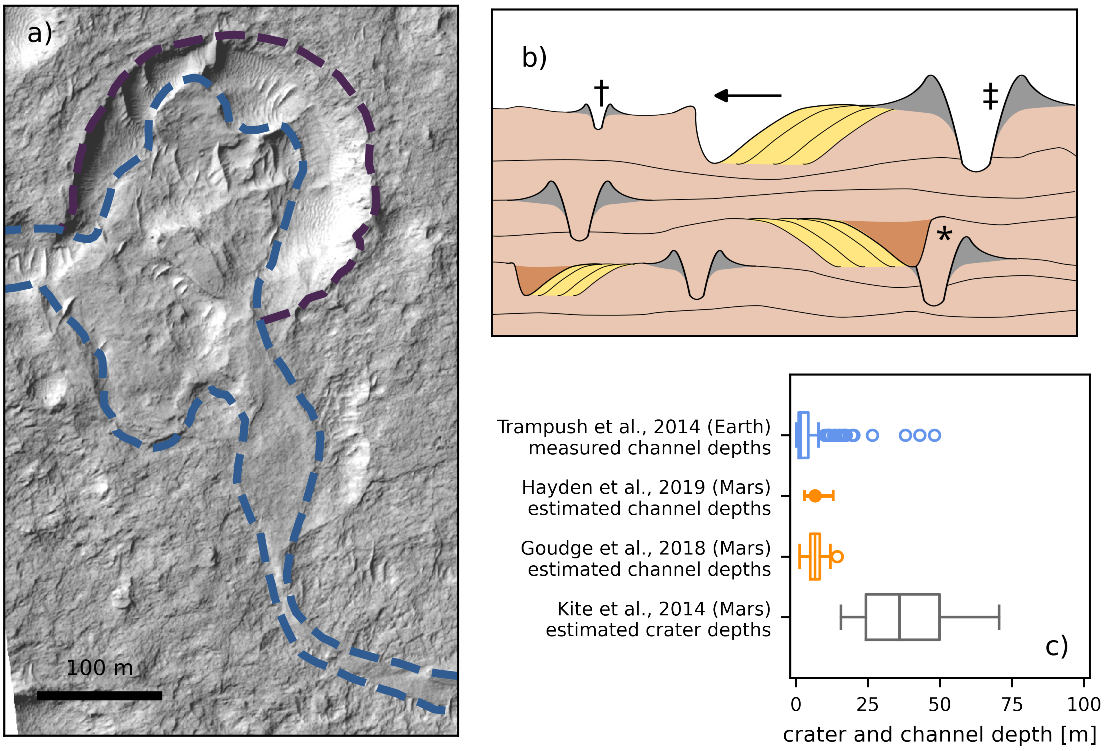

Figure 1. a) Example of a 238 m diameter crater (purple dashed line) interbedded with fluvial deposits (blue dashed lines) identified by Kite et al. (2013). Crater is located in the Aeolis Dorsa region, Mars (153.803E, 5.991S; HiRISE image ESP_017548_1740; NASA/JPL-Caltech/UArizona; McEwen et al., 2007). b) Schematic cross-section of channel and crater interactions in the production of stratigraphy. The ← marks the migration direction of a channel located at the surface, which was steered by a larger crater rim marked by the ‡. The † indicates a crater rim that may be removed from the record due to ongoing channel migration and the relative size of the channel and crater rim. In contrast, the larger crater rim (‡) is unlikely to be removed, due to its position relative to the migration direction and larger size. In the stratigraphy, there are several fully preserved channel lateral migration deposits, and a crater rim that is partially preserved (marked by *), due to erosion by a migrating channel. c) Channel and crater depths on Earth and Mars (Trampush et al., 2014; Goudge et al., 2018; Hayden et al., 2019) have similar absolute scales to depths of craters missing from the ancient stratigraphic record on Mars, which has been used to estimate paleo-atmospheric pressure (Kite et al., 2014); here, a boxplot characterizes a distribution, and the solid circle and bar indicates a mean and range.

2013; Wickert et al., 2013; Straub et al., 2015; Hajek & Straub, 2017). For example, a deeper channel reaches farther into the subsurface and erodes sediment over a larger cross-sectional area, and a more rapidly migrating or avulsing channel increases the proportion of the landscape visited and where stratigraphy is destroyed. Moreover, whether a fluvial system is dominated by channel migration or avulsion is also known to affect stratigraphic reworking (Straub et al., 2009; Wang et al., 2011), with dominance between the two mobility modes being related to, among other factors, sediment composition (Straub et al., 2015; Liang et al., 2015a, 2016; Hajek & Straub, 2017). Finally, the fluvial system aggradation rate also affects stratigraphic reworking, because slower aggradation keeps sediments near the surface and within reach of channels for an increased duration (Hajek & Straub, 2017).

Coincidentally, typical river channel depths have similar absolute scales to smaller crater depths (Figure 1b,c). For example, typical alluvial river channel depths range 1–5 m on Earth (Trampush et al., 2014) and are estimated to have been 2–10 m on Mars (Goudge et al., 2018; Hayden et al., 2019), and crater depths range $<$1–20 m for craters $\lesssim$50 m in diameter. Notably, initial crater depths of craters measured by Kite et al. (2014) would have been mostly deeper than estimated channel depths (Figure 1c), opening the possibility that the "missing" smaller craters were removed from the record by migrating river channels, and therefore not observed when strata were later exhumed and interbedded crater sizes were mapped (Kite et al., 2014). Moreover, it is known that ancient channels moved across the Mars landscape when the stratigraphic interval of interest was produced (Goudge et al., 2018; Hayden et al., 2019; Cardenas & Lamb, 2022).

Overlapping absolute dimensions of fluvial channels and smaller craters raise the possibility that fluvial reworking has removed a substantial portion of smaller interbedded craters from the Mars stratigraphic record. Indeed, if fluvial reworking substantially biased the Mars crater record, the lack of smaller craters would not be a robust proxy for atmospheric paleo-pressure (Kite et al., 2014). Warren et al. (2019) applied an analytical size-dependent filter to approximate crater removal by sedimentary processes and investigate if these processes could meaningfully change paleo-pressure interpretations. Their study determined that the process-filter could not explain the observed Mars crater record, but the functional form and parameterization of the analytical filter were not calibrated or validated. We hypothesize that fluvial activity can rework and eliminate from the stratigraphic record crater deposits that form proximally to river channels (i.e., interbedded craters).

We further hypothesize that because smaller craters ($\lesssim$50 m diameter) present a less significant physical obstacle to a laterally migrating or avulsing river than larger craters ($\sim$50–300 m diameter), there is a crater size-dependent bias in the removal of craters by fluvial reworking. This preferential removal of smaller craters would adjust atmospheric paleo-pressure interpretations downwards, by confirming the possibility that unobserved crater diameters were eliminated by fluvial reworking, rather than by atmospheric ablation.

In this study, we answer the question: can fluvial reworking explain the lack of smaller interbedded craters ($\lesssim$50 m) on Mars? We first forward modelled coeval river-delta evolution and crater production, and assessed preservation of craters within the fluvial-deltaic stratigraphy. With these observations, we studied how crater size-frequency distributions are impacted by fluvial reworking, and determine how to account for this bias when making atmospheric paleo-pressure interpretations.

2 Modeling crater production and delta sedimentation

We simulated river-delta development with coeval crater production using open-source research software. We use Python 3.9.5 and *pyDeltaRCM* v2.1.4 for delta modeling (Moodie et al., 2021), and coupled it with crater size-frequency distributions generated with *craterstats2* v3.0.11 (Michael et al., 2016), and an analytical framework describing fresh crater geometries (A. D. Howard, 2007). Our workflow is fully reproducible, and all modeling and analysis codes are archived, with links to repositories in the Open Research Section.

2.1 Crater size-frequency distributions

The accumulated history of crater production and destruction is recorded in crater size-frequency distributions (CSFDs). Most commonly, a crater size-frequency distribution (CSFD) is measured over a control area and used to constrain surface age (e.g., Fassett, 2016). This approach com-

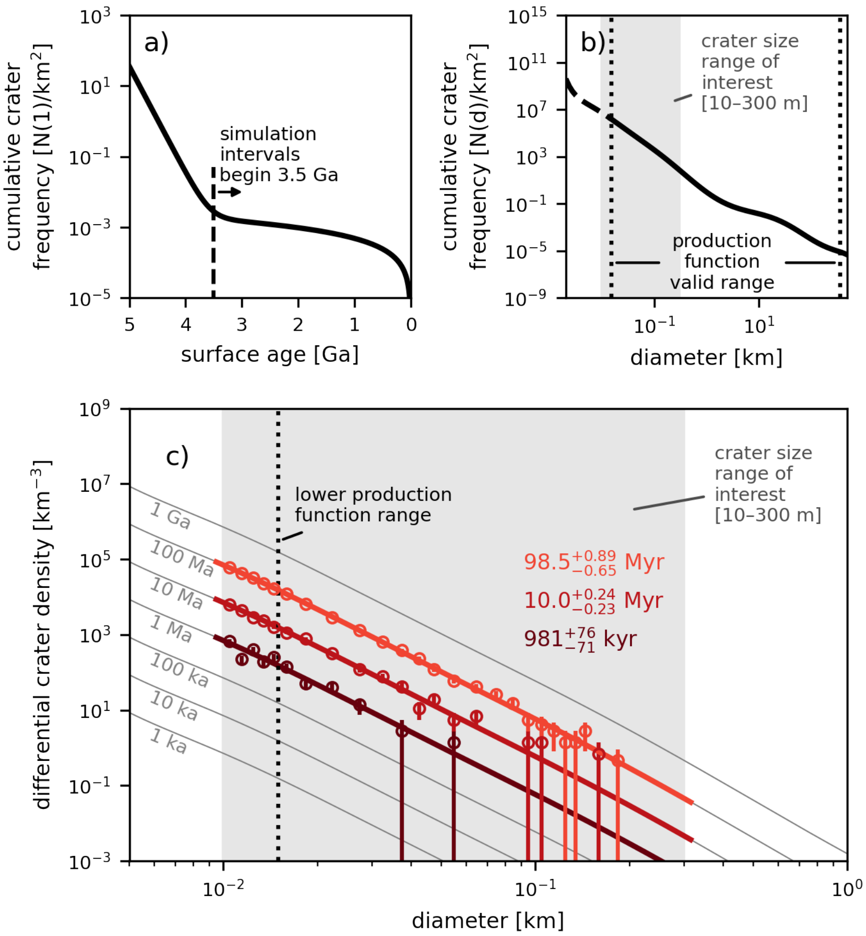

Figure 2. a) The Hartmann and Neukum (2001) Mars chronology function, describing the number of 1 km diameter craters per km^2, accumulated on a surface with a given age. b) The Ivanov (2001) Mars production function, describing the relative abundance of craters by diameter. c) The chronology function and production function are used together in a Monte Carlo simulation to generate crater-size populations representing time durations of 1 Ma, 10 Ma, and 100 Ma, and beginning 3.5 Ga, which are then used in model simulations (see text for additional details; Michael et al., 2016).

pares the measured CSFD to modeled CSFDs that would be expected for surfaces with different ages. Modeled CSFDs are made by combining an expected proportionality of craters of different sizes (a so-called "production function") with an estimate of past crater production rates (a so-called "chronology function"). Production and chronology functions are calibrated for the Moon, and are extended to other celestial bodies, including Mars (Ivanov, 2001).

We synthesized crater size-frequency distribution samples for our coupled delta-cratering model via Monte Carlo simulation, following the approach of Michael et al. (2016). We selected the Hartmann and Neukum (2001) Mars chronology function and Ivanov (2001) Mars production function for simulation. Monte Carlo simulations begin during the era of vigorous hydrological activity on ancient Mars at 3.5 Ga (Fassett & Head, 2008; Hoke & Hynek, 2009; Mangold et al., 2012), and include craters in the diameter range 10–300 m. Notably, the lower bound of our crater size range of interest extends beyond the size range of our chosen production function (Figure 2b; Ivanov, 2001); over this extrapolated diameter range, the slope of the production function is consistent with diameters within the function valid range (Figure 2b).

Monte Carlo simulation proceeds by choosing a crater size from a uniform probability distribution over the size range of interest, and determining the instantaneous cratering rate for that crater size from the chronology and production functions. The time to the next cratering event depends on the selected crater size, such that over many crater iterations, the synthesized crater size-frequency distribution conforms with the production function, and the distribution is consistent with a specified amount of elapsed time (Figure 2c). We specify CSFDs that represent elapsed time of 1, 10, and 100 Myr for simulations (Figure 2c).

We limited crater production to diameters less than 300 m because larger features can generate morphodynamic instability in the numerical delta model. We expect that this is a reasonable upper bound for craters that may be partially reworked by fluvial activity, but are unlikely to be completely eliminated from the stratigraphic record; this assumption will be tested with simulations.

2.2 Delta model

Coeval delta and crater production was simulated with the *pyDeltaRCM* numerical model (Moodie et al., 2021), which is a flexible implementation of the widely used DeltaRCM delta model (Liang et al., 2015a). DeltaRCM model design has been robustly validated (Liang et al., 2015a, 2015b, 2016) and used to examine delta morphology and evolution under various external forcings and processes (Lauzon & Murray, 2018; Lauzon et al., 2019; Piliouras et al., 2021; Moodie & Passalacqua, 2021; Hariharan et al., 2021, 2022, 2023). In this article, we do not describe the complete model implementation, and instead provide a high-level overview that highlights model components relevant to our study design and interpretations; a full model description is given in Liang et al. (2015a).

In DeltaRCM, a deltaic landform emerges from rules that iteratively route water and sediment via weighted random walk, from a fixed inlet location and into an initially empty receiving basin (Figure 3a; Liang et al., 2015a). Water is steered primarily by topographic gradients, moving down-gradient, and sediment is routed according to topographic and hydrodynamic gradients, with weighting that varies between the two for different sediments (Liang et al., 2015a; Wright et al., 2022). In this way, the routing rules were developed with "just enough" complexity to yield realistic fluvial-deltaic channel dynamics, so that the model maintains simplicity and computational efficiency (Liang et al., 2015a). Importantly, the dependence of water and sediment routing on topography is the fundamental connection between crater formation and delta evolution, and ultimately crater preservation or removal. DeltaRCM creates both fluvial and deltaic deposits simultaneously across the model domain (Hariharan et al., 2021); we do not differentiate between these depositional styles in assessing reworking bias, and discuss some potential implications of deltaic versus fluvial processes on our results in Section 4.3).

We did not modify any model routing rules for this study, including adjustments to the effect of gravity (Supplementary Materials; e.g., Braat et al., 2021, 2024). The gravitational acceleration constant is parametrically linked to only a partitioning coefficient that plays a role in water routing (γ; Supplementary Materials). Additional processes in the model are conceptually dependent on the gravity, but do not have physics-based parametric links to the gravitational acceleration constant (e.g., sediment entrainment and suspension thresholds; Braat et al., 2024). Nevertheless, because the DeltaRCM model is governed by feedbacks between flow and topography, and these feedbacks are first-order processes in morphodynamics on Mars as well, we are confident the model can be applied to study crater preservation on Mars; other science applications of the model on Mars may require a careful sensitivity and parameter analysis (e.g., Braat et al., 2021, 2024).

DeltaRCM is known to be underestimate non-local and backwater hydrodynamic effects that develop upstream of channel bifurcations and obstructions (Liang et al., 2015b). As a result, water and sediment are erroneously transported up-slope in some uncommon circumstances where flow energy is especially high; in that case, high topography outside of channels may be unrealistically lowered. This model idiosyncrasy leads to craters erroneously classified as having been partially reworked, but is a relatively rare occurrence, so we do not expect a significant impact on our results.

The mixture of sediment grain sizes input to a river delta is known to impact delta morphology and dynamics (Edmonds & Slingerland, 2010), and this dependence is borne out in DeltaRCM as well (Liang et al., 2015a, 2016; Hariharan et al., 2021; Moodie & Passalacqua, 2021). In DeltaRCM, the sediment mixture is controlled by a "sand fraction" parameter that shifts the mixture from muddy to sandy, and therefore transitions the delta between two modes of channel mobility. Channels in muddy simulations are generally stable, exhibiting a single active channel with moderate local lateral migration of channel bends, that is punctuated by large delta-scale lobe-switching avulsions that swiftly relocate the channel across the delta. In contrast, sandy simulations maintain multiple simultaneously-active channels that extensively migrate and frequently avulse across the landscape at multiple spatial scales (Liang et al., 2015a). Additionally, muddy simulations exhibit higher surface roughness, that is, higher average elevation variation across the landscape (Liang et al., 2016), which means that avulsions in muddy simulations develop new channels unevenly and in deep topographic lows, whereas avulsions in sandy simulations distribute sediment more evenly across the landscape. Importantly, this change in surface channel mobility translates to increased reworking of sedimentary deposits and stratigraphy for sandy simulations, relative to muddy simulations (Hariharan et al., 2021).

pyDeltaRCM uses a flow intermittency assumption to represent only morphodynamically active time, and therefore decrease model computation time. This common modeling assumption (e.g., Parker, 2004) is based on the nonlinear relationship between water and sediment discharge, and the increasing rarity of flows of increasing magnitude (Wolman & Miller, 1960). In essence, there is a river discharge that moves significant sediment volumes and occurs frequently, such that this discharge is treated as the meaningful control on the long-term evolution of the landform; only this discharge is modeled and is scaled to represent elapsed total time. Flow intermittency on Mars is poorly constrained (Stucky de Quay et al., 2021; Buhler et al., 2014), so model design simply assumes that significant flow intervals are evenly distributed over the duration of the simulation (e.g., not randomly distributed, but divided evenly over 100 Myr of elapsed total time).

In our simulations, water and sediment debouch into the 6 m deep receiving basin from a 6 m deep and 150 m wide channel at 1,350 m^3/s and 1.35 m^3/s discharge, respectively. The model uses a grid spacing of 20 m, over a 6×12 km domain. Simulations use a moderate sediment composition value, with equal parts sand and mud (i.e., sand fraction value is 0.5), which is within the broad range of grain size mixtures observed on Earth and Mars (J. P. Grotzinger et al., 2015; Stack-Morgan et al., 2023). These simulation parameters lead to development of channels 118 ± 68 m wide and 7 ± 3 m deep (mean $\pm$ standard deviation) that exhibit dynamics consistent with real-world terrestrial systems (Liang et al., 2015a, 2016). We ran simulations for 10,000 timesteps, which amounts to 107×10^6 seconds of intermittent bankfull river flow. Parameters and domain scaling were selected based on prior experience with numerical stability in the model, and minimal deviation from a set of parameters commonly used with DeltaRCM (e.g., Liang et al., 2015a; Lauzon & Murray, 2018; Lauzon et al., 2019; Piliouras et al., 2021; Moodie & Passalacqua, 2021; Hariharan et al., 2021,

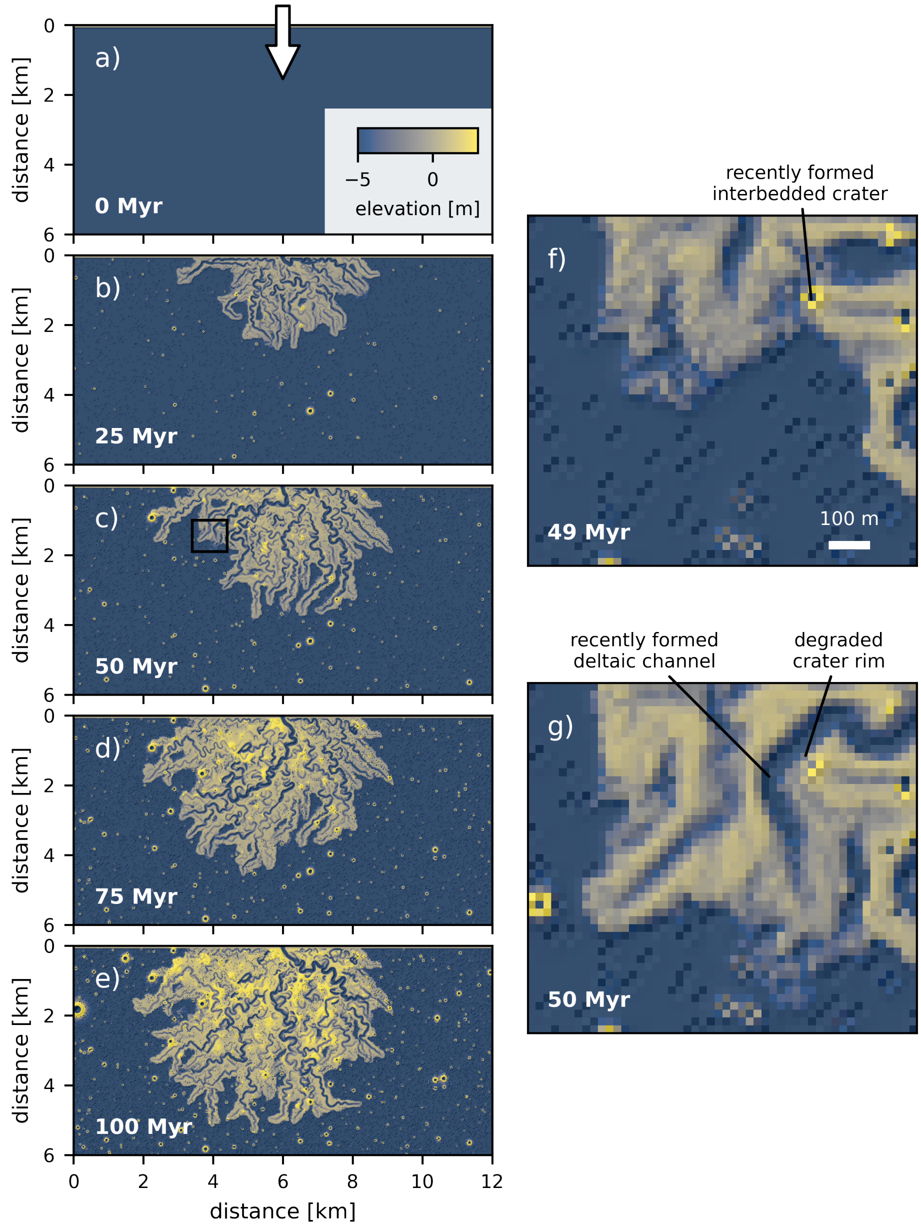

Figure 3. a–e) Timeseries of coeval river-delta and crater production for one 100 Myr simulation; color from blue to yellow highlights delta elevation. f–g) Highlight from timeseries at 49 to 50 Myr, showing a fluvial channel formed via avulsion and the associated partial degradation of an older crater ∼20 m in diameter; location of highlighted area is shown by black square in panel c.

2022, 2023). At the end of the simulation, deposits extend 4–5 km into the basin and span 8–10 km perpendicular to the inlet channel (Figure 3e), therefore maintaining an approximately axis-symmetric planform over many cycles of channel movement (Parker et al., 1998; Reitz & Jerolmack, 2012; Moodie et al., 2019).

The model domain size and initial configuration, with a flat basin and single narrow inlet (Figure 3a) is conceptually consistent with a delta forming on the floor of a large crater (>30 km diameter) from an inlet valley cutting across the crater rim. Notably, delta deposits at the end of simulation (Figure 3e) scale similarly to the Jezero Crater western delta deposits (e.g., Fassett & Head III, 2005; Goudge et al., 2018), though we did not explicitly attempt to model these deposits.

2.3 Coupling cratering and the delta model

Before beginning a simulation, we generate a crater-size distribution commensurate to the timescale of interest (e.g., 100 Myr) and determine independent crater formation times (i.e., cratering is a random Poisson process Herkenhoff & Plaut, 2000; Michael et al., 2016). Craters are placed between delta-model timesteps (Figure 3a–e), and are located randomly within the model domain but rectified to the model grid. Fresh crater geometry is generated according to (A. D. Howard, 2007), with the modification that ejecta deposits are not modeled beyond 6× the crater radius. Crater formation is instantaneous, and has no effect on sediment erodibility in the delta model. Craters $\lesssim$40 m (i.e., $\lesssim$2× the grid spacing; Shannon, 1949) have shorter rim heights in our model than dictated by A. D. Howard (2007), due to grid discretization effects (Supplementary Materials). This discretization effect could artificially increase the ability of smaller modeled craters ($\lesssim$ 30 m) to be removed, versus larger craters. However, because channel depths overwhelm crater rim heights in this size range, we do not expect discretization effects to affect our conclusions (Supplementary Material).

Each crater rim and ejecta deposit is tagged with a unique identifier, so that these materials are identifiable in the final modeled stratigraphy (Figure 4b). Rim material is labeled from $0.9r \leq x < 1.41r$, where r the crater radius and x is distance from the crater center, and crater ejecta is labeled from from $1.41r \leq x \leq 6r$. A single exception is that a minimum one-cell-wide annulus is created around a minimum one-cell central crater-floor cell; i.e., for the smallest craters, there is a single crater-floor cell with the eight surrounding neighbor cells marked as crater rim deposits. Rim and ejecta locations are tagged when craters are formed, and recorded to the model output intermittently. We use *DeltaMetrics* to convert timeseries model outputs to a gridded stratigraphic volume with 10 cm vertical resolution. *DeltaMetrics* determines the time when a given grid elevation was last occupied by the sediment surface at that location (Schumer et al., 2011), and assigns each voxel within the stratigraphic volume to reflect the appropriate simulation conditions. This approach creates a temporal discretization bias, that is minimized by saving model states at a high temporal resolution with respect to landscape evolution (e.g., Moodie et al., 2021; Moodie & Passalacqua, 2021; Hariharan et al., 2023).

Simulations do not include any additional surface processes that would eliminate crater deposits or obfuscate crater rims and reduce mappability, including for example, diffusive rim degradation by wind, water, or subsequent impactors (Öpik, 1966; Hartmann, 1966; Ross, 1968; Soderblom, 1970; Hartmann, 1971; Schultz & Gault, 1975; Hartmann & Neukum, 2001; A. Howard, 2004; Richardson et al., 2004, 2005; M. R. Smith et al., 2008; Richardson, 2009; Minton et al., 2015). However, our model implicitly includes crater obliteration by direct overprinting from subsequent craters (Woronow, 1977, 1978; Minton et al., 2015); we determined there to be little effect on our results from crater obliteration (Supplementary Material). Moreover, our modeling represents a

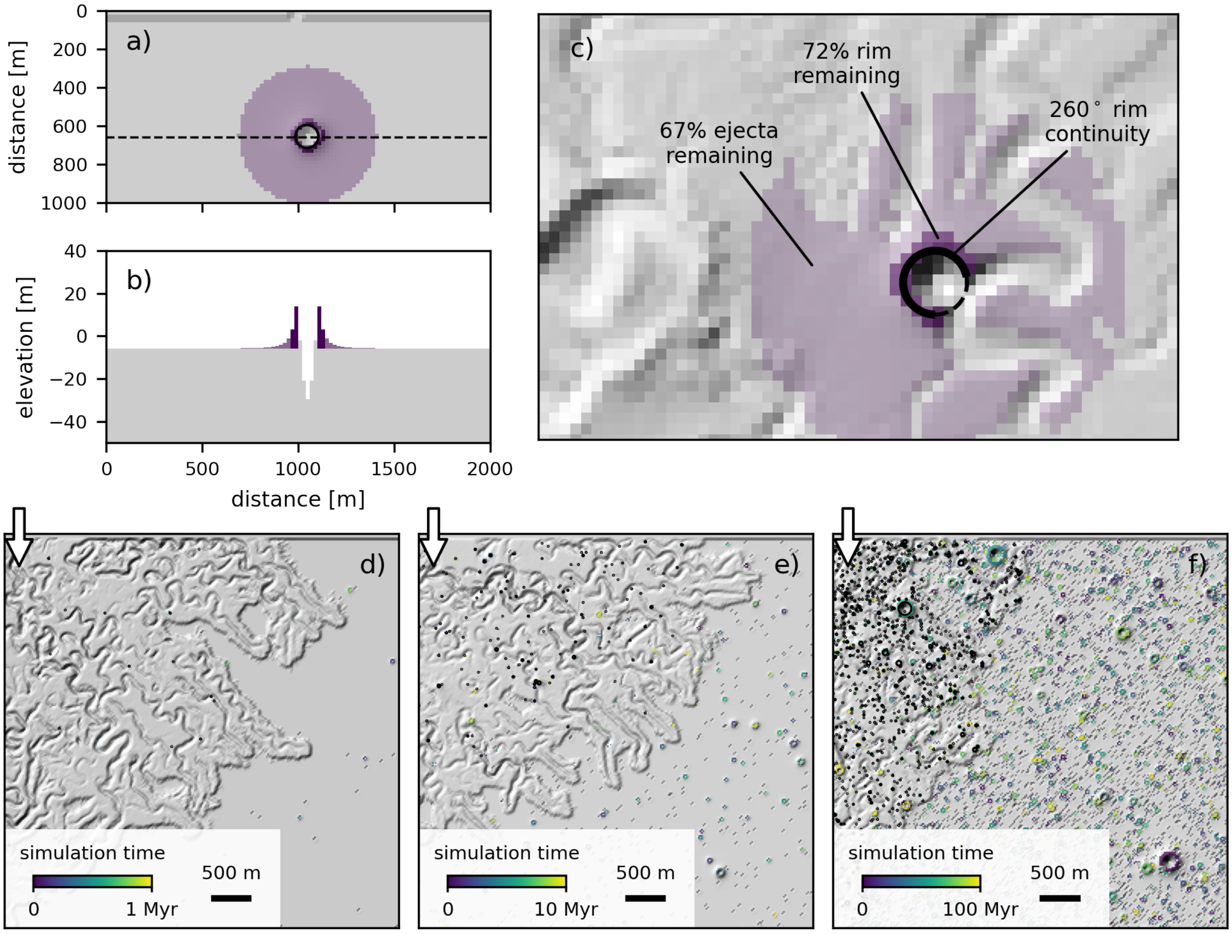

Figure 4. Example of a single pristine crater in a) mapview and b) cross-section, showing the extent of deposits tagged as crater rim (dark purple) and crater ejecta (light purple). c) Example of crater rim and ejecta degraded by fluvial reworking, and study metrics evaluated for this degraded crater. Topographic hillshade of a d) 1 Ma, e) 10 Ma, and f) 100 Ma simulation. Crater rim material *at the deposit surface* is colored by crater formation time, with black circles highlighting interbedded crater rims. The area of each panel is $\sim$27 km^2 (approximately half of the model domain, with white arrows indicating the channel inlet location.

net-depositional environment, and so assessment of crater removal in this study is not applicable to net-erosional valley networks on Mars, or locations without any evidence for fluvial and deltaic sedimentation.

We ran nine replicate simulations for each of 1 Myr, 10 Myr, and 100 Myr (27 simulations total) to assess uncertainty and develop a large number of craters for analyses (180,844 craters). Model replicates for a given delta formation timescale (e.g., all 100 Myr replicates) used different crater-size distributions synthesized by Monte Carlo simulation.

3 Results

3.1 Crater rims and ejecta preserved in stratigraphy

Landscape development over time (Figure 3) generates stratigraphy that includes fluvial deposits and crater rim and ejecta material (Figure 4). From 180,844 craters across all formation duration and replicate simulations, we identified 26,709 interbedded craters. Iterating over each crater, we identified the initial crater deposit annulus area (i.e., excluding the crater floor), separated the rim and ejecta material, and calculated 1) the remaining fraction of rim annulus area, 2) the remaining fraction of ejecta annulus area, and 3) the angle subtended by the largest contiguous segment of the rim annulus remaining (e.g., Figure 4c). For calculation of the remaining rim fraction for a single crater, for example, we divide the number of model grid cells that include rim material from that crater at any height in the stratigraphic column, by the number of grid cells that were initially marked as containing crater rim material for that crater; the remaining ejecta fraction is calculated in the same manner. Calculation of the preserved rim continuity similarly identifies grid cells with stratigraphic columns including rim material of that crater, and bins these cells into azimuthal ranges with respect to the crater center, and determines the arc length of the largest sector of consecutive bins. Identifying crater rim and ejecta material anywhere in the stratigraphic volume, rather than only exposed at the surface, isolates metrics from the effects of exhumational bias (Warren et al., 2019).

All metrics are impacted by model grid discretization effects, but these effects are most apparent for smaller craters, and for the rim fraction and rim continuity metrics. This sensitivity arises because smaller crater rims occupy only eight grid cells immediately surrounding a single crater-floor grid cell, which creates, for example, just nine possible quanta for the preserved rim fraction $(0, 0.125, \ldots, 0.875, 1.0$; Figure 5a); in some rare circumstances, time discretization effects introduce additional possible quanta (Supplementary Material).

For crater diameters from 10 to $\sim$50 m, the fraction of crater rim and ejecta area preserved varies between 0.0 and 1.0 (i.e., fully eroded to fully preserved), and this variability decreases as crater diameter increases, generally converging towards full preservation (Figure 5a,b). Preserved rim continuity is similarly variable for smaller crater diameters ($\lesssim$50 m), and converges towards 360° continuity with increasing crater diameter (Figure 5c). Importantly, robust trends in preservation for larger diameter craters in the size range of interest (150–300 m) are obscured by the fact that simulations included only seven craters larger than 150 m, due to the nature of crater production functions (e.g., Figure 2; Ivanov, 2001).

Non-overlapping 25 m crater diameter bin averages (gray boxes, Figure 5a–c) show a broad increase in preservation with increasing crater diameter. Approximately 67% of smaller interbedded-crater rims ($\lesssim$50 m) have been at least partially eroded (measured as rim continuity $<$360°), with 38% having less than half of the rim area remaining, and 44% having less than 180° of preserved rim continuity. Interestingly, about 53% of larger interbedded-crater rims (crater diameter $>$50 m) were also partially eroded (measured as rim continuity $<$360°), with 19% and 24% having less than half rim fraction preserved and less than 180° preserved rim continuity, respectively. Overall, simulations indicate that fluvial reworking can erode a substantial fraction of interbedded crater rims, especially affecting smaller crater rim deposits.

Preservation does not depend on the crater accumulation time duration (Figure 5d), or on crater formation time (Figure 5a–c). When preserved rim continuity data are separated into simulations representing 1, 10, and 100 Ma and summarized as 25 m-bin averages (Figure 5d), the trend of each simulation duration set is not distinguishable from the others. Most importantly, for smaller

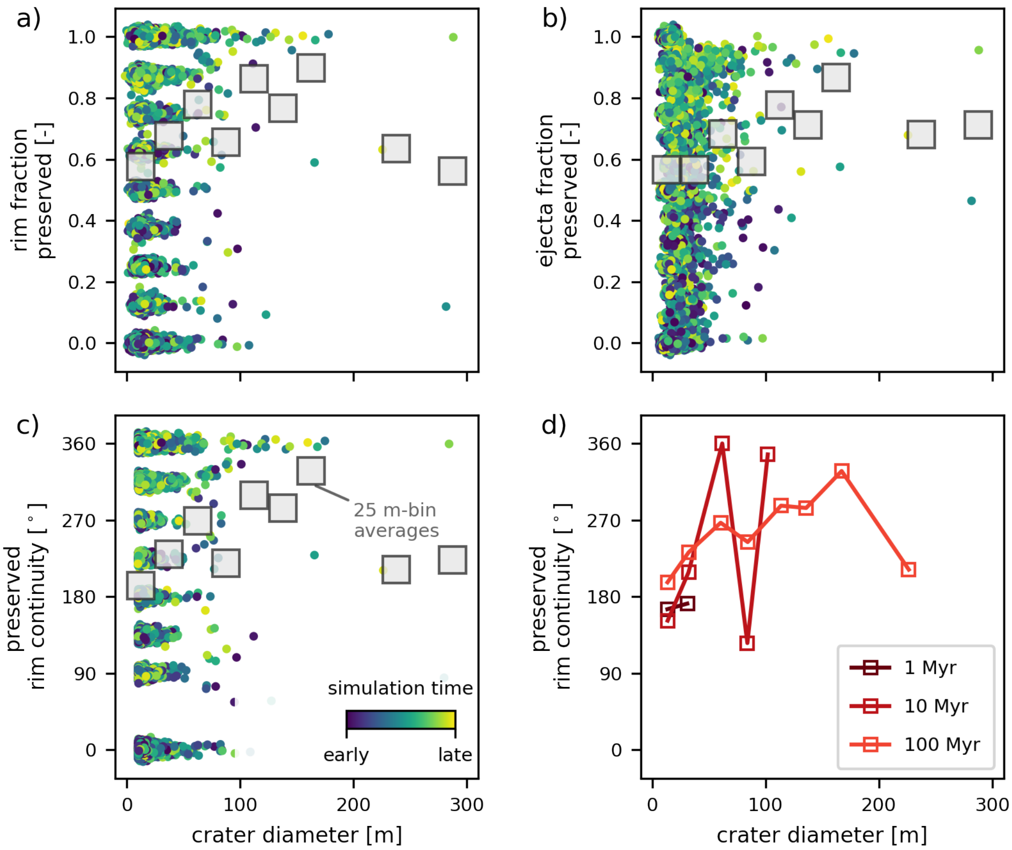

Figure 5. Interbedded crater a) rim fraction preserved, b) ejecta fraction preserved, and c) preserved rim continuity as a function of crater diameter, and colored by crater formation time within a simulation. Data are aggregated across all simulation timescales and replicates, and have normally-distributed noise added to both axes for visualization (mean of 0, and standard deviation of ± 0.01 or $\pm 1.5^{\circ}$, and ± 1.5 m). Gray boxes mark non-overlapping 25 m-bin averages. d) 25 m-bin averages of preserved rim continuity separated by simulation duration. Total number of craters accumulated (i.e., simulation duration) does not impact the fluvial reworking bias.

diameter craters ($\lesssim$50 m) where data density sufficiently characterizes fluvial reworking bias, there is little difference in rim continuity for different simulation durations (Figure 5d).

3.2 Biased crater size-frequency cumulative distributions

We made synthetic fluvial reworking-biased crater diameter distributions by Monte Carlo sampling from the simulated crater record, and compare biased distributions to the full interbedded crater distribution, and to the observed Mars interbedded crater distribution (e.g. Kite et al., 2014). To generate a CSFD biased by fluvial reworking, we randomly selected 56 craters from the simulated interbedded crater record (56 is the number of craters observed in the Kite et al. (2014) dataset), and excluded those craters with $<180^{\circ}$ rim continuity. We repeated this process 100 times to assess distribution variability, and show the median distribution, and 16$^{\text{th}}$ to 84$^{\text{th}}$ percentile distributions in cumulative probability space, as a solid line and shaded envelope, respectively (Figure 6). Cumulative distributions are useful to visually highlight (dis)similarity of two distributions as (non)overlapping

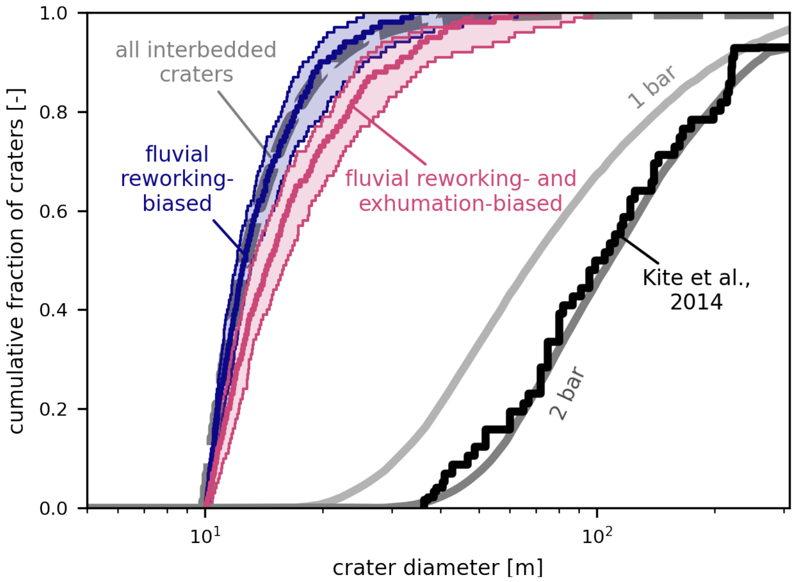

Figure 6. Empirical crater size distributions of all modeled interbedded craters (dashed gray line), preserved and mappable craters after applying fluvial reworking bias (blue) and fluvial plus exhumation biases (pink), and interbedded craters mapped by Kite et al. (2014) (solid black line); results are compared to crater size distributions predicted for paleo-atmospheric pressures (solid gray lines) from (Kite et al., 2014). For preserved and mappable crater size distributions, the biases applied are fluvial reworking (blue), and fluvial plus exhumational bias (pink). Calculated distributions are shown by the median (solid line), and envelope from the 16th to 84th percentile distributions (shaded area).

lines when plotted (Figure 6); differences in either distribution support (left-to-right shifts) or density (curve and slope change) create perceptual dissimilarity. Synthetic distributions reflect a set of "mappable" craters, which are those with rim preservation above a threshold value and anywhere in the simulated stratigraphic volume; we include craters embedded within the stratigraphy to isolate the fluvial reworking effect on crater distributions. We note that a $<180°$ rim continuity threshold was also used by Kite et al. (2014) to map craters on Mars, but Warren et al. (2019) excluded craters with $<150°$ of topographically elevated rim (including discontinuous sections); we thresholded based on continuous rim arc length because it is considerably simpler to implement for automatic calculation than other crater metrics. Sensitivity testing revealed that differences in the threshold (120°–240°) and the number of craters (40–72) do not impact results.

The cumulative distributions biased by fluvial reworking are similar to the cumulative distribution of all interbedded craters (Figure 6). Additionally, there is little variability among the sampled fluvial reworking-biased distributions (i.e., between the 16th and 84th percentile distributions; Figure 6). The sampled fluvial reworking-biased distributions have a distinct range and density from the Kite et al. (2014) observed crater diameter distribution (Figure 6). For example, the fluvial reworking-biased distributions are dominated by crater diameters 10–20 m approximately following an exponential distribution, whereas the observed data approximately follows a one-sided truncated normal distribution with the smallest observed diameter ∼35 m (Figure 6).

In addition to fluvial reworking, measured interbedded crater-size distributions are biased by exhumational processes that preferentially expose larger craters buried within stratigraphy (Kite et al., 2013). Preferential exhumation is due to geometric constraint that a quasi-horizontal plane cutting through a rock volume will sample features from the volume proportional to the features' length scale along the axis normal to the quasi-horizontal plane (Russ, 1986; Yielding et al., 1996). Assuming semi-hemispherical craters with a fixed ratio between crater diameter and depth (e.g., Melosh, 1989), the proportion of craters sampled on a quasi-horizontal plane is therefore dependent on crater depth (i.e., the vertical crater length; Lewis & Aharonson, 2014), or following the fixed depth-diameter ratio, crater exhumation bias is proportional to crater diameter (Kite et al., 2014). Our study examines crater rim and ejecta deposits, and we similarly assume a fixed ratio between crater depth and rim height, such that exhumation bias is linearly proportional to crater diameter. Note, the crater depth/height-to-diameter ratio is not explicitly included in the proportionality, so the relevant assumption is just that this ratio is fixed over the size range of interest.

We model exhumation bias by applying an increased weighting to larger craters in Monte Carlo sampling to generate synthetic crater diameter distributions from simulations. Probability for a crater with diameter d to be included in the synthetic distribution goes as $p(d) \propto d/d_{min}$, where $d_{min} \approx$10 m is the smallest crater diameter in the simulations. We empirically tested whether exhumational bias follows this proportionality, and determined that it is a reasonable first-order approximation of the bias imparted by exhumation, but that bias depends on the relative rate of deposit accumulation and crater production, and assumptions of crater geometry (Section 4.4.3; Supplementary Materials).

Cumulative distributions biased by fluvial reworking and exhumation have a marked increase in larger craters, with respect to the distribution of all interbedded craters (Figure 6). Still, the distributions are dominated by 10–30 m diameter craters, and remain substantially different in shape and scale from the observed crater-size distribution (Figure 6).

4 Discussion

4.1 Fluvial reworking bias does not explain observed crater populations

Despite nearly half of smaller craters ($\lesssim$50 m) having $<180^\circ$ remaining rim continuity and potentially not being mappable, the shift in the cumulative CSFD due to fluvial reworking is very small (Figure 6). This small shift arises because the CSFD is dominated by smaller craters: there are $\sim$340 times more interbedded and mappable ($>180^\circ$ rim continuity) craters sized 5–15 m than sized 55–65 m (18,743 and 55 craters, respectively). The relative abundance of smaller craters is a factor of the crater production function, and although the true crater production function is unknown, the approximately exponential form of the function is not disputed (Fassett, 2016). So, although fluvial reworking can remove many smaller craters, the dominance of smaller craters in the CSFD is inescapable, and fluvial reworking cannot bias the crater record to the extent needed to explain observed distributions. Notably, even in the extreme case of a delta formed over 1 Myr, which leads to the smallest number of accumulated craters (Figure 2), fluvial reworking does not modify the CSFD enough to match observations on Mars (Figure 5d; Supplementary Material).

Our findings are consistent with previous studies that hypothesize fluvial reworking is not a primary control on observable crater size-frequency distributions of ancient interbedded craters on Mars (Kite et al., 2014; Warren et al., 2019). Our results indicate that fluvial reworking is a subordinate control because of the overwhelming number of smaller craters generated, rather than the notion that crater deposits are not eliminated from the stratigraphic record (indeed, many crater deposits are eliminated by fluvial reworking; e.g., Figures 3 and 5). Though lateral migration and avulsion place channels across the entire delta over time, channels occupy only a small fraction of the delta surface at any moment in time (Reitz & Jerolmack, 2012), such that the majority of new interbedded craters are formed away from active channels. Interestingly, a crater must be at least partially buried by fluvial sediments to be considered an interbedded crater for this study, so it appears that craters formed away from active channels receive distally deposited fine sediment, but that many crater locations must not be revisited by a channel during the simulation. In summary, our simulations show that fluvial reworking, by way of lateral migration and avulsion, is not able to remove smaller craters at the pace they are created.

Our conclusions bolster studies that use the lack of smaller interbedded craters as evidence for a higher pressure ancient atmosphere. In contrast to migrating rivers that intermittently visit locations on the landscape, a planetary atmosphere exists everywhere above the landscape and is in place to brake and ablate all incoming impactors. For example, in the case of an atmosphere with stable pressure, there is a lower limit to the diameter of impactors that survive atmospheric ablation, translating to a lower limit on crater diameters formed (Kite et al., 2014). Though paleo-pressure may have fluctuated in the past (Warren et al., 2019), we see very little possibility for atmospheric pressure to have remained low enough for long enough that a substantial number of smaller craters would have formed *and* subsequently be eliminated by fluvial reworking. Instead, a more likely scenario is that the smaller craters never formed, due to higher atmospheric pressure. Moreover, the sustained and intense fluvial activity that would be needed to rework enough smaller craters to reproduce observed distributions would be highly unlikely without at least some atmosphere (e.g., Kite, 2019; Kite et al., 2022), which would therefore inhibit formation of smaller craters in the first place. In summary, simulation results indicate that although rivers are sometimes in the right place to remove smaller craters, an atmosphere is always in place to remove small impactors and prevent formation of smaller craters altogether.

4.2 The functional form of the fluvial reworking filter

Although fluvial reworking cannot account for the lack of smaller interbedded craters observed on Mars, our modeling results indicate that fluvial erosion can remove a significant proportion of these craters from the stratigraphic record. Creating a well-calibrated crater removal function could bolster atmospheric paleo-pressure interpretations. Moreover, a set of calibrated crater removal functions could be used to infer characteristics of ancient river migration and avulsion, for example, from divergences between observed CSFDs and those predicted for atmospheric filtering from an independently constrained paleo-pressure. It would be problematic to calibrate a crater removal function from our simulation results heretofore, because simulations include a limited number of larger interbedded crater observations (only seven craters $\gtrsim$150–300 m; Figure 5). The limited number of larger craters is a realistic constraint, imposed by the nature of crater production in the solar system (e.g., Figure 2b,c; Ivanov, 2001), but relaxing this constraint could refine our view of crater reworking over the complete range of crater sizes of interest (10–300 m).

4.2.1 Uniform crater size-frequency distribution simulations

To increase observations of interbedded craters $\gtrsim$150 m in diameter, We ran additional simulations with a uniform crater size-frequency distribution (i.e., craters of all diameters 10–300 m are equally likely). Simulation parameters otherwise remained the same as previous simulations, except for two modifications. First, we limited the number of craters per simulation to 250 and increased the number of replicate simulations, because too many larger craters in a single simulation introduced numerical instability to the delta model. Second, we varied sediment composition input to the delta (Liang et al., 2016; Moodie & Passalacqua, 2021), to assess how channel mobility modulates the fluvial reworking filter. We varied the input sediment mixture from a muddy to sandy composition

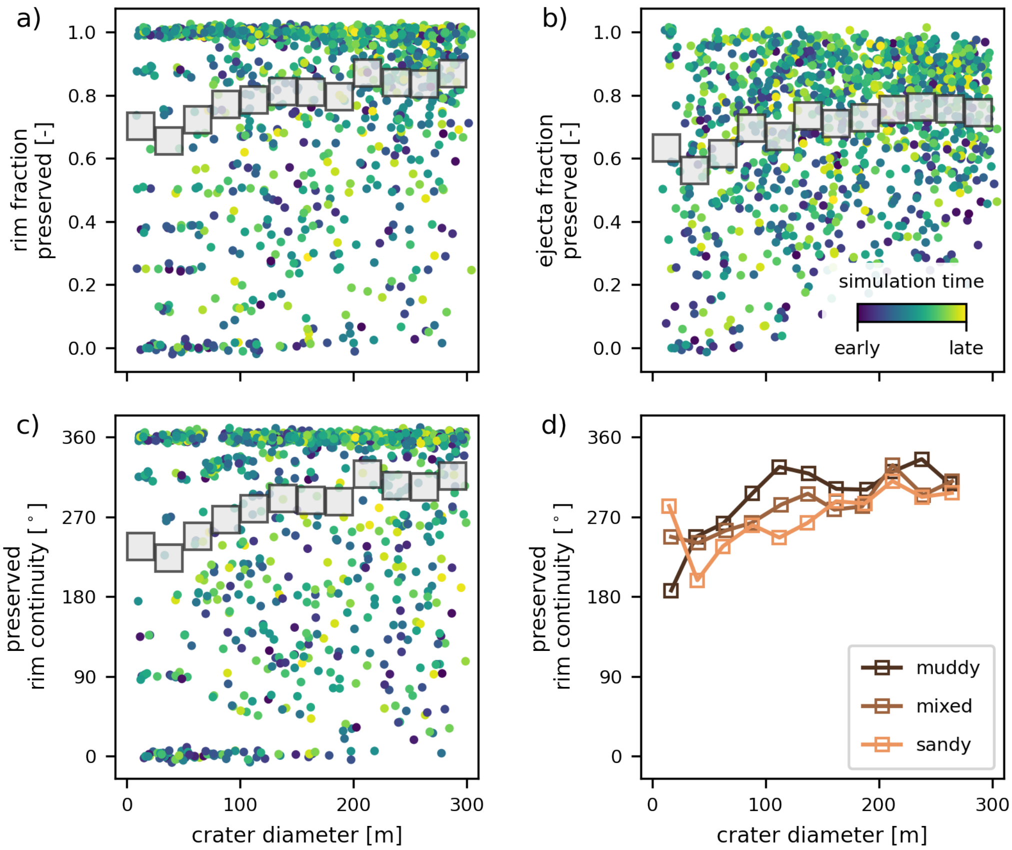

Figure 7. Interbedded crater a) rim fraction preserved, b) ejecta fraction preserved, and c) preserved rim continuity as a function of crater diameter for uniform crater size-frequency distribution. Data are aggregated across all input sediment compositions and replicates, and up to ±0.1 or ±1.5° and ±1.5 m point jitter is added for visualization. Gray boxes mark mutually exclusive 25 m-bin averages. Calculated metrics show that preservation is varied, but on average increases with increasing crater diameter. d) 25 m-bin averages of preserved rim continuity separated by sediment composition input to the delta. Increasing input sandiness led to a decrease in preserved rim continuity, i.e., an increase in fluvial reworking bias.

(sand fraction 0.2, 0.5, and 0.8) across 36 runs (12 replicates for each sand fraction), yielding 9000 craters and 1180 interbedded craters to examine preservation metrics (Figure 7). Sediment composition is known to influence channel dynamics and the resultant bias in stratigraphic preservation (e.g., Straub et al., 2015), so this parameter is highly relevant to our study and will set first-order bounds on plausible interbedded crater reworking.

We computed the rim fraction preserved, ejecta fraction preserved, and rim continuity in the same manner as previous simulations (Figure 7a–c). Similar to size-frequency distribution simulations, uniform size distribution simulations indicate varied preservation, ranging from undegraded craters to complete removal. 25 m-bin averages indicate that preservation generally increases with crater size (Figure 7a–c). Notably, uniform size distribution simulations characterize average fluvial reworking bias more smoothly and over a more complete crater diameter range than size-frequency distribution simulations (Figures 5 and 7).

Splitting simulations by input sediment composition reveals differences in average preservation of smaller crater deposits (Figure 7d). Muddy simulations resulted in higher preservation than sandy simulations on average (Figure 7d). Average preservation in muddy simulations shows a non-linear dependence on crater diameter (with preservation dropping steeply below $\lesssim$100 m), whereas sandy simulations have an approximately linear dependence on crater size (Figure 7d). As described in Section 2.2, DeltaRCM simulations of sandy deltas have higher rates of channel mobility and therefore increased sediment reworking relative to muddy deltas (Liang et al., 2015a; Hariharan et al., 2021). Differences in fluvial reworking for different sediment compositions are second order to the size-dependent trend, and are consistent with a process-based understanding of channel dynamics and stratigraphic preservation (Hajek & Straub, 2017; Hariharan et al., 2021).

4.2.2 Calibrating a function for crater removal by fluvial reworking

We define a filtering function, representing the average bias applied to the interbedded crater record by fluvial reworking:

$$c = (1 - c_0)\left[1 - \exp\left(\frac{(d_0 - d)}{n}\right)\right] + c_0, \tag{1}$$

where c is the fraction of craters of diameter d remaining, c_0 is a reference crater fraction remaining when $d \to 0$, d_0 is a reference crater diameter, n is an "e-folding" crater diameter. The functional form of the filter is after the Warren et al. (2019) crater removal factor, and is augmented with a reference term c_0 to represent the fraction of craters preserved as $d \to 0$. Values of c_0 are bounded in $[0,1]$, values of d_0 are bounded in $[0,\inf)$ (Warren et al., 2019), and Equation 1 is only valid for $d > 0$, such that values of c are always in $[0,1]$. Note that when $c_0 = 0$, the original filter function of Warren et al. (2019) is recovered.

The constraint that d_0 characterize a reference crater diameter ≥ 0 forces the average remaining crater fraction c to be zero for $d \geq 0$ (i.e., full reworking reached at some crater diameter greater than or equal to zero, Figure 8). However, there is no empirical evidence or theory that indicates full reworking should be a requirement of the fluvial filter. Indeed, our empirical simulations show only partial reworking for the smallest crater diameters (e.g., $c > 0$ as $d \to 0$; Figure 7), and therefore do not support the constraint imposed by the d_0 reference diameter. One option would be to allow d_0 to take a negative value, but the physical meaning of a negative reference diameter is not clear. Instead, we choose to augment the filter function with the c_0 term, to ensure $d_0 \geq 0$ and enable partial reworking as $d \to 0$.

Figure 8 shows Equation 1 determined with parameters from Warren et al. (2019) for Meridiani ($c_0 = 0$, $d_0 = 15.7$, $n = 23$), and for parameters determined from regression for our simulation results. For regression, we determine mappable fraction as the 25 m-bin averages of interbedded craters from the uniform crater size-frequency distribution simulations with rim continuity $\geq 180°$, and treating the muddy and sandy simulations separately (i.e., data are after Figure 7c). We used the uniform crater size-frequency distribution simulation results for regression because these results characterize average crater preservation across the crater size range of interest; only seven craters $\gtrsim$150–300 m were observed in the simulations using the Ivanov (2001) crater size-frequency distribution (Figure 5). Using different simulation results would yield different parameters for Equation 1, but we expect the model form would remain the same (e.g., compare figures 5 and 7). We defined the mappable crater fraction using the rim continuity data because this metric is commonly used as a threshold criteria in crater counting (Kite et al., 2014; Warren et al., 2019), and other metrics would be difficult to constrain outside of the model. Finally, we set $d_0 = 0$ and estimate c_0 and n only, because c is non-uniquely dependent on c_0 and d_0 (Equation 1). Model parameters determined for muddy simulations are $c_0 = 0.46 \pm 0.09$, $d_0 = 0$, and $n = 78 \pm 18$, and are $c_0 = 0.63 \pm 0.04$, $d_0 = 0$, and $n = 288 \pm 76$ for the sandy simulations; $\pm$ represent 1σ values.

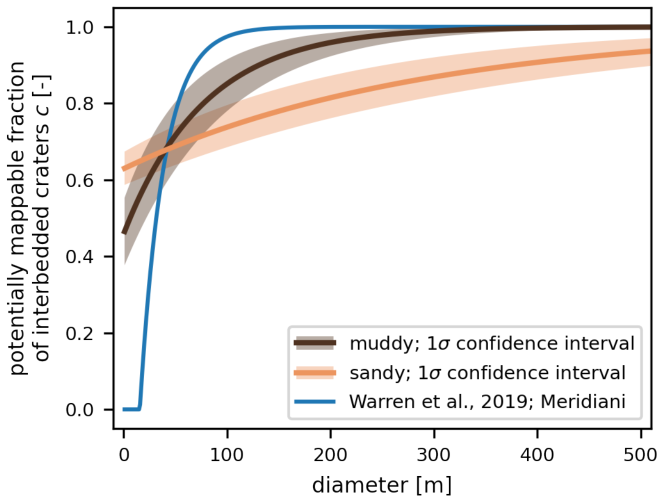

Figure 8. Potentially mappable fraction of interbedded craters as a function of crater diameter. The blue curve is Equation 1 with parameters from Warren et al. (2019) for Meridiani ($c_0 = 0$, $d_0 = 15.7$, $n = 23$). The brown and orange curves and shaded areas are Equation 1 evaluated with model parameters and 1σ confidence intervals for muddy and sandy simulations, respectively. Data used to determine parameters are 25 m binned averages fraction of craters preserved with $\geq 180°$ rim continuity, and therefore includes buried craters (i.e., excludes exhumation bias).

The filter proposed by Warren et al. (2019) captures the nature of the relationship between fluvial reworking and average crater preservation, but their parameterization underestimates the range over which reworking occurs, and overestimates the degree to which reworking changes with crater diameter (Figure 8). Our calibrated models have a larger e-folding crater diameter (n), and because we set $d_0 = 0$ and determine c_0, our parameterizations maintain a proportion of potentially mappable craters (i.e., $c > 0$) at even the smallest crater diameters. Differences in crater preservation patterns between the muddy and sandy simulations lead to distinct estimated parameters for these sedimentological systems (Figure 8), though difference due to sediment input is small with respect to the difference from the Warren et al. (2019) parameterization. Estimated values of n characterize the sensitivity of reworking to change in crater diameter in Equation 1, with smaller values of n representing increased sensitivity in muddy simulations.

4.2.3 Implications and potential applications of the crater removal function

Fluvial reworking bias can be accounted for where a sufficient density of interbedded craters is present, and Equation 1 can therefore bolster atmospheric paleo-pressure interpretations. For example, Equation 1 can integrate into an inference framework that improves atmospheric paleo-pressure estimates, by considering the observed CSFD as it is found, after being biased by atmospheric filtering and fluvial reworking (in that order). This framework would shift interpreted paleo-pressure upper-bounds (e.g., Kite et al., 2014; Warren et al., 2019) to now-lower paleo-pressure estimates with meaningful uncertainty; for example, CSFDs modeled for different atmospheric pressures and fluvial reworking would steepen and rotate counter-clockwise, becoming increasingly convex-up at smaller diameters. We emphasize that our estimated fluvial reworking filter characterizes the fraction of craters preserved *on average* (with a measure of variability), and so any revised paleo-pressure interpretations using this filter should carry uncertainty due to variability (Figure 8). Additionally, our estimated fluvial reworking filter implicitly incorporates the effects of crater obliteration during formation of new craters, and so may slightly overestimate the effect of fluvial reworking bias alone (Supplementary Materials); we cannot separate crater obliteration from fluvial reworking in our simulations, as is the case in natural systems. To be complete, an inversion framework should incorporate additional crater-degrading surface processes and possible sources of bias (exhumation bias has already been incorporated in these frameworks; Kite et al., 2014); but importantly, we do not expect these factors to significantly impact crater counts (Section 4.4). Finally, it is worth reiterating that our filtering model (Equation 1) is only applicable in net-depositional environments, and is not applicable in net-erosional valley networks on Mars, or locations without any evidence for fluvial and deltaic sedimentation.

Details of sediment composition and channel characteristics that prevailed on ancient Mars are not well constrained (J. P. Grotzinger et al., 2015; Stack-Morgan et al., 2023), so model-fit parameterizations should be interpreted as scenarios that estimate a plausible range of reworking bias. Interestingly, it may be possible to infer ancient channel dynamics from mapped CSFDs if atmospheric paleo-pressure is independently constrained. For example, the crater-diameter range over which the observed crater size-frequency distribution deviates from the known paleo-pressure expected distribution, could inform whether ancient channel dynamics were more similar to dynamics of channels in muddy or sandy simulations.

4.3 Crater removal determined by channel avulsion frequency and channel geometry

We interpret the difference in average preservation between muddy and sandy simulations to be due to varied channel mobility modes and varied channel geometry between the cases, which are well known to be modulated by the sand fraction input to DeltaRCM (Section 2.2; Liang et al., 2015a, 2016; Moodie & Passalacqua, 2021). To briefly summarize simulation differences, muddy simulations exhibit narrower and deeper channels that remain in place longer before delta-scale avulsions relocate channels, whereas sandy simulations maintain shallower and wider channels that frequently avulse at multiple scales. These model behaviors are consistent with a process-based understanding of controls on channel geometry (Dunne & Jerolmack, 2018; Dong et al., 2019; Dunne & Jerolmack, 2020) and avulsion (Mohrig et al., 2000; Slingerland & Smith, 2004; Straub et al., 2015).

We originally hypothesized that larger craters ($\sim$50–300 m diameter) have rims rising above the delta plain that would present a physical obstacle to flow, and therefore not be reworked and removed from the stratigraphic record. Our results repeatedly document a crater diameter-dependent bias (e.g., Figures 5 and 7), and here we interpret observed crater preservation patterns in the context of hypothesized topographic steering. It is important to emphasize that differences between muddy and sandy preservation are only apparent in *average* behavior (Figure 7d, Figure 8), and that both cases exhibit varied preservation ranging from craters that are fully eliminated to fully preserved.

Channel avulsions cause flow to spread across the delta landscape, generally following topographic gradients to a new outlet on the coast (Jerolmack & Paola, 2007; Reitz et al., 2010). In our simulations, flow during avulsion is steered by self-organized delta topography and by crater topography; an example of flow steered by self-organized topography during an avulsion is shown in Figure 3f–g. Infrequent avulsions in muddy simulations create significant self-organized topographic roughness (e.g., Liang et al., 2016), such that if flow encounters crater topography during an avulsion, it may be steered towards a nearby topographic low, wherein a new channel is formed (e.g., Figure 3f–g). Frequent avulsions in sandy simulations distribute sediment more evenly across the deltaic landscape, such that topographic lows are rapidly filled and topographic variability is relatively small (e.g., Liang et al., 2016). Therefore, when an avulsion occurs in sandy simulations, flow is not easily steered by crater topography towards a topographic low (i.e., because there are no significant topographic lows). The effect of these differences, on average, is that the overall crater removal fraction is higher in sandy simulations (Figure 8), and crater removal is less sensitive to crater size in sandy simulations (Figure 8). Said another way, the presence of topographic lows in muddy simulations enhances the size-dependent bias that removes smaller craters from the crater record, but reduces reworking overall.

From a geometric perspective, fluvial reworking occurs where a channel cross-section intersects with deposited sediments, and so is limited to the landscape area visited by channels, and extends into the subsurface down to the channel depth. This perspective implies that more frequent avulsions would increase fluvial reworking, and also that deeper channels would increase fluvial reworking. Sandy simulations, which have shallower channels and more frequent avulsions than muddy simulations, exhibit higher average reworking. This indicates that crater deposit reworking is more sensitive to avulsion frequency than channel depth. We expect that processes influencing crater removal in uniform crater size-frequency distribution simulations also modulate reworking in our primary simulations with CSFDs synthesized from a production function. Reworking in primary simulations is likely transitional between reworking observed in end-member muddy and sandy simulations, because the input sand fraction value in these simulations is between the muddy and sandy sand fraction values.

There are some additional factors of the model design and simulation configurations that could affect reworking. Reworking could increase in a situation where a river or delta is confined by valley walls, because a higher proportion of the active fluvial area (i.e., floodplain) is occupied by channel area (Dong & Goudge, 2022). By similar logic, braided rivers that occupy a larger fractional area of the active fluvial area (Tejedor et al., 2022; Dong & Goudge, 2022) could show a higher proportion of crater reworking. Thus, we would expect the number of intersections between interbedded craters and channel cross sections to increase, thereby enhancing crater removal. Additionally, river bend migration in confined valleys can be dominated by down-valley bend translation that eliminates strata over the full valley width (Limaye & Lamb, 2013). However, it is not currently known whether Aeolis Dorsa, or other paleo-channel features were formed in confined valleys or on broad alluvial plains (Cardenas et al., 2017; Dong & Goudge, 2022). Separately, erodibility of deposits surrounding craters or ejecta material following crater formation is not changed in our model. For example, heat from crater formation can increase hardness of the crater substrate, impact energy transferred to substrate material can cause fracturing, and ejecta may have a lower bulk density than the crater substrate, depending on the impactor and target materials (Melosh, 1989). Finally, we did not modify model processes and mechanisms to reflect changes in environmental constants, such as the gravitational acceleration constant (Section 2.2). Although we assume the model can be reasonably applied to understand fluvial reworking and crater size bias (Section 2.2, Supplementary Material), future research into differences in the mechanics of Earth and Mars rivers and deltas could challenge that assumption.

4.4 Degradation, obliteration, exhumation, and image resolution as potential sources of bias

Crater degradation is the erosion of crater rims and infilling of crater floors by sedimentary processes, so that crater topographic expression is gradually diminished over time (Craddock et al., 1997; Forsberg-Taylor et al., 2004; M. P. Golombek et al., 2014). We did not include any crater degradation effects in our model, so a natural question is whether including these processes, in conjunction with fluvial reworking bias, could meaningfully impact the observable smaller crater record on Mars. In this section, we examine several processes and effects that alter crater topography on ancient and modern Mars. We comment on whether these processes could impact modeling results, and speculate on how sensitive counting of interbedded craters on Mars is to these processes.

4.4.1 Wind and aeolian erosion

M. P. Golombek et al. (2014) found that aeolian erosion degrades recently formed smaller crater rims on modern Mars at up to 1 m/Myr, but that this rate quickly declines to 0.1 m/Myr; longer-term rates are as low as 0.001 m/Myr (M. P. Golombek et al., 2006). Aeolian sedimentation rates during the period of fluvial activity of interest beginning 3.5 Ga are poorly constrained, but modern rates of erosion serve as a helpful proxy for the following thought experiment. For a crater rim height to diameter ratio of $\sim$0.04 (Pike, 1977; Melosh, 1989; Robbins & Hynek, 2012), we expect freshly formed crater rims $<$1 m high for craters smaller than 30 m. This rim height is sufficiently small that wind-blown degradation rates up to 1 m/Myr could substantially weather craters before entering the stratigraphic record.

Our simulations spanned a range of plausible delta formation timescales 1, 10, and 100 My (Bhattacharya, 2005; Buhler et al., 2014; Irwin et al., 2015; Lapôtre & Ielpi, 2020). In the extreme case of a delta forming intermittently over 100 My and aeolian erosion occurring at similar rates to modern craters, a crater formed on the delta surface would be weathered for several million years before a channel returns to the area to potentially bury the crater deposit (Figure 3). In such a situation, it is possible that smallest-crater rims could be substantially degraded before being incorporated into the stratigraphic record, and therefore be unrecognizable as craters after exhumation. At more moderate timescales of delta formation and lower crater degradation rates, we do not anticipate that crater rims would be substantially degraded before potential incorporation into the stratigraphic record. Future modeling could consider how craters of varying degrees of degradation are incorporated into the stratigraphic record and later exhumed as landforms observable on the modern Mars surface (e.g., Cardenas et al., 2022). Importantly, even if wind degrades all or a significant fraction of craters below 30 m before burial, our conclusions would not change, because mappable cumulative crater-size distribution shape would likely still be dissimilar to Mars observations (e.g., Figure 6).

4.4.2 Crater obliteration

Obliteration of an existing crater rim or ejecta deposit by the formation of a new impact crater leads to a steady state crater size-frequency distribution, which deviates at smaller crater diameters from the distribution dictated by the crater production function (Woronow, 1977, 1978; M. R. Smith et al., 2008; Richardson, 2009; Minton et al., 2015). This crater obliteration processes is implicitly included in our simulations, though our simulations accumulate far fewer craters than needed to approach a steady state distribution. Nevertheless, we ran nine simulations without river-delta sediment input, and then generated craters according to 100 Myr of elapsed time beginning 3.5 Ga, and quantified preservation using the same routine as the main text. In these simulations, we find that smaller craters are preferentially rendered unmappable by obliteration (consistent with prior research), but that the magnitude of crater removal by obliteration is far less than fluvial reworking, and therefore does not affect our study interpretations. For example, crater obliteration removes $\sim$10% of crater rim area for craters $\lesssim$50 m, $\sim$10% of crater ejecta area for all crater sizes modeled, and similarly minimally impacts the preserved rim continuity. Importantly, these obliteration metrics represent upper bounds on crater obliteration bias, because craters remain at the modeled surface and there is no mechanism to incorporate crater material into stratigraphy and away from the surface new craters form on.

We do not expect that Mars interbedded crater records are significantly affected by crater obliteration during formation of new craters. Interbedded craters would have formed on active sedimentary surfaces that would not have persisted long enough for an equilibrium density of craters to form.

4.4.3 Exhumational bias of larger craters

Exhumational bias preferentially exposes larger craters, when a sedimentary volume with interbedded craters is eroded (Kite et al., 2013). To represent this process in our analysis, we relied on previous research that presents a geometry-based theory for how this bias impacts crater size-frequency distributions (Lewis & Aharonson, 2014). We attempted to empirically validate this theory in the course of our research, and found that the theory provides an acceptable first-order approximation of the effect. Still, we determined that there is an opportunity for further research to improve our understanding of exhumational bias in crater records (Supplementary Material).

In any case, we do not expect that plausibly enhanced exhumational bias would impact our primary conclusion that fluvial reworking cannot reproduce observed Mars crater-size distributions. Our attempts to validate the exhumational bias theory indicate that the level of bias needed to remove enough smaller craters to explain the observed Mars crater record is not plausible. Importantly, an improved understanding of exhumational bias will be necessary to incorporate the fluvial reworking process into inference frameworks (e.g., Section 4.2.3).

4.4.4 Image and data resolution

Crater mappabilty is affected by horizontal and vertical image resolution, as well as image illumination angles (Williams et al., 2018). Craters smaller than 3$\times$ data resolution (dx) are not reliably mapped (Richardson, 2009), which provides a reasonable estimate of the lower bound of potentially mappable craters in any dataset. Crater measurements generated by Kite et al. (2014) used HiRISE images (0.25–0.5 m/pixel) that yield gridded digital terrain models (DTMs) with approximately 2–3 m horizontal resolution, and vertical precision on the order of tens of centimeters (McEwen et al., 2007; Beyer et al., 2018). Freshly-formed crater rim heights are approximately 4% of the crater diameter (Robbins & Hynek, 2012), so craters $\geq$5 m would have rim heights $\geq$20 cm, and can be reasonably expected to be mappable in DTMs derived from HiRISE imagery. Therefore, we do not expect data resolution to impact mappable crater counts in previous Mars studies, but CSFDs generated without high-resolution images are unlikely to generate reliable paleo-atmospheric pressure estimates.

As mentioned previously, embedded craters that become exposed at the surface by exhumation could be degraded by aforementioned modern sedimentary processes (i.e., wind-blown erosion). Interestingly, these processes could render craters that are fully preserved in the fluvial reworking sense, to become unmappable at present day, due to post-exhumation erosion that lowers observable rim heights below image resolution thresholds. We cannot rule out that modern erosion of ancient interbedded craters affects mappable crater distributions on Mars (Williams et al., 2018), but also do not expect this effect to invalidate upper-bound paleo-pressure interpretations, because including potentially omitted smaller craters would lower upper-bound estimates.

5 Conclusions

In this study, we perform a quantitative evaluation of the potential for fluvial reworking of sedimentary deposits to impart a size-dependent bias on crater size-frequency distributions. Our modeling approach reveals that as many as 67% of smaller craters ($\lesssim$50 m diameter) are at least partially eroded, with 38–44% of smaller craters having less than half the initial deposit remaining, and that preservation of craters is highly variable. Notably, average crater preservation decreases with decreasing diameter, confirming the presence of a size-dependent fluvial reworking bias. However, the nature of crater size-frequency distributions (i.e., an approximately exponential increase in crater frequency with decreasing diameter) creates a condition where fluvial reworking cannot remove enough smaller craters to meaningfully bias interbedded crater records. That is to say, although fluvial reworking preferentially removes smaller crater deposits from the stratigraphic record, there are too many smaller craters produced for preserved crater size-frequency distributions to meaningfully change. This conclusion ultimately bolsters paleo-pressure studies that rely on these interbedded crater records. We developed a function that predicts the average fraction of craters removed by fluvial reworking, and determined parameters of the function for simulations exhibiting varied channel dynamics. Specifically, we observe that simulations with more sand input remove more crater rims overall, but with reduced size-dependent bias; we interpret these observations as being controlled by changes in avulsion frequency and topographic relief that depend on input sediment composition. Overall, our findings bolster studies that assert fluvial reworking is not a primary control on smaller interbedded crater counts on Mars.

Open Research Section

All data, custom model scripts, and analysis scripts used in this research are archived on the corresponding author's Github page at https://github.com/amoodie/paper_resources in a folder titled "Moodie_marscraterreworking". The Github repository and versioned copies of all models and bespoke software used in this research is additionally archived in a Zenodo repository (doi 10.5281/zenodo.10050333).

Acknowledgments

The authors gratefully acknowledge David Mohrig for helpful conversations that guided this research. We are also grateful to two anonymous reviewers for their thoughtful comments and suggestions that greatly improved our manuscript. A.M. was supported by a Jackson School of Geosciences Postdoctoral Fellowship at the University of Texas at Austin.

References

Beyer, R. A., Alexandrov, O., & McMichael, S. (2018). The ames stereo pipeline: Nasa's open source software for deriving and processing terrain data. *Earth and Space Science*, *5*(9), 537–548. doi: 10.1029/2018EA000409

Bhattacharya, J. P. (2005). Dynamic river channels suggest a long-lived noachian crater lake on Mars. *Geophysical Research Letters*, *32*(10). Retrieved from `https://doi.org/`

10.1029/2005gl022747 doi: 10.1029/2005gl022747

Bishop, J. L., Fairén, A. G., Michalski, J. R., Gago-Duport, L., Baker, L. L., Velbel, M. A., ... Rampe, E. B. (2018, February). Surface clay formation during short-term warmer and wetter conditions on a largely cold ancient Mars. *Nature Astronomy*, *2*(3), 206–213. doi: 10.1038/s41550-017-0377-9

Braat, L., Brückner, M. Z. M., Sefton-Nash, E., & Lamb, M. P. (2024). Gravity-driven differences in fluvial sediment transport on mars and earth. *Journal of Geophysical Research: Planets*, *129*(2). doi: 10.1029/2023JE007788

Braat, L., Lamb, M., & Sefton-Nash, E. (2021). Differences between deltas on earth and mars.. Retrieved from https://essopenarchive.org/doi/full/10.1002/essoar.10509327.1 doi: 10.1002/essoar.10509327.1

Bridge, J. S., & Mackey, S. D. (1992). A theoretical study of fluvial sandstone body dimensions. In *The geological modelling of hydrocarbon reservoirs and outcrop analogues* (pp. 213–236). John Wiley & Sons, Ltd. doi: 10.1002/9781444303957.ch14

Buhler, P. B., Fassett, C. I., Head, J. W., & Lamb, M. P. (2014, October). Timescales of fluvial activity and intermittency in milna crater, Mars. *Icarus*, *241*, 130–147. doi: 10.1016/j.icarus.2014.06.028

Cabrol, N. A., Grin, E. A., Newsom, H. E., Landheim, R., & McKay, C. P. (1999). Hydrogeologic evolution of gale crater and its relevance to the exobiological exploration of Mars. *Icarus*, *139*(2), 235–245. doi: 10.1006/icar.1999.6099

Cardenas, B. T., & Lamb, M. P. (2022, October). Paleogeographic reconstructions of an ocean margin on Mars based on deltaic sedimentology at aeolis dorsa. *Journal of Geophysical Research: Planets*, *127*(10). doi: 10.1029/2022je007390

Cardenas, B. T., Lamb, M. P., & Grotzinger, J. P. (2022, October). Martian landscapes of fluvial ridges carved from ancient sedimentary basin fill. *Nature Geoscience*, *15*(11), 871–877. doi: 10.1038/s41561-022-01058-2

Cardenas, B. T., Mohrig, D., & Goudge, T. A. (2017, 09). Fluvial stratigraphy of valley fills at Aeolis Dorsa, Mars: Evidence for base-level fluctuations controlled by a downstream water body. *GSA Bulletin*, *130*(3-4), 484–498. doi: 10.1130/B31567.1

Craddock, R. A., Maxwell, T. A., & Howard, A. D. (1997). Crater morphometry and modification in the sinus sabaeus and margaritifer sinus regions of Mars. *Journal of Geophysical Research: Planets*, *102*(E6), 13321–13340. doi: 10.1029/97JE01084

Day, M., Edgett, K. S., & Stumbaugh, D. (2019, December). Ancient stratigraphy preserving a wet-to-dry, fluvio-lacustrine to aeolian transition near barth crater, arabia terra, Mars. *Journal of Geophysical Research: Planets*, *124*(12), 3402–3421. doi: 10.1029/2019je006226

Dong, T. Y., & Goudge, T. A. (2022, 06). Quantitative relationships between river and channel-belt planform patterns. *Geology*, *50*(9), 1053–1057. doi: 10.1130/G49935.1

Dong, T. Y., Nittrouer, J. A., Czapiga, M. J., Ma, H., McElroy, B., Il'icheva, E., ... Parker, G. (2019, January). Roles of Bank Material in Setting Bankfull Hydraulic Geometry as Informed by the Selenga River Delta, Russia. *Water Resources Research*, *55*(1), 827–846. doi: 10.1029/2017WR021985

Dunne, K. B. J., & Jerolmack, D. J. (2018). Evidence of, and a proposed explanation for, bimodal transport states in alluvial rivers. *Earth Surface Dynamics*, *6*(3), 583–594. doi: 10.5194/esurf-6-583-2018

Dunne, K. B. J., & Jerolmack, D. J. (2020). What sets river width? *Science Advances*, *6*(41), eabc1505. doi: 10.1126/sciadv.abc1505

Edmonds, D. A., & Slingerland, R. L. (2010, February). Significant effect of sediment cohesion on delta morphology. *Nature Geoscience*, *3*(2), 105–109. doi: 10.1038/ngeo730

Edwards, M. B., & Eri, K. A. (1983). Paleochannel geometry and flow patterns determined from exhumed permian point bars in north-central texas. *SEPM Journal of Sedimentary Research*, *Vol. 53*. doi: 10.1306/212f835a-2b24-11d7-8648000102c1865d

Fassett, C. I. (2016). Analysis of impact crater populations and the geochronology of planetary surfaces in the inner solar system. *Journal of Geophysical Research: Planets*, *121*(10), 1900–1926. doi: 10.1002/2016JE005094

Fassett, C. I., & Head, J. W. (2008, May). The timing of Martian valley network activity: Constraints from buffered crater counting. *Icarus*, *195*(1), 61–89. doi: 10.1016/j.icarus.2007.12.009

Fassett, C. I., & Head III, J. W. (2005). Fluvial sedimentary deposits on Mars: Ancient deltas in a crater lake in the nili fossae region. *Geophysical Research Letters*, *32*(14). doi: 10.1029/2005GL023456

Forsberg-Taylor, N. K., Howard, A. D., & Craddock, R. A. (2004). Crater degradation in the Martian highlands: Morphometric analysis of the sinus sabaeus region and simulation modeling suggest fluvial processes. *Journal of Geophysical Research: Planets*, *109*(E5). doi: 10.1029/2004JE002242

Frazier, D. E. (1967). Recent deltaic deposits of the Mississippi River: their development and chronology. *Transactions of the Gulf Coast Association of Geological Societies*, *27*, 287–315.

Ganti, V., Straub, K. M., Foufoula-Georgiou, E., & Paola, C. (2011). Space-time dynamics of depositional systems: Experimental evidence and theoretical modeling of heavy-tailed statistics. *Journal of Geophysical Research: Earth Surface*, *116*(F2). doi: 10.1029/2010JF001893

Golombek, M., Robinson, K., McEwen, A., Bridges, N., Ivanov, B., Tornabene, L., & Sullivan, R. (2010). Constraints on ripple migration at meridiani planum from opportunity and hirise observations of fresh craters. *Journal of Geophysical Research: Planets*, *115*(E7). doi: 10.1029/2010JE003628

Golombek, M. P., Grant, J. A., Crumpler, L. S., Greeley, R., Arvidson, R. E., Bell III, J. F., ... Squyres, S. W. (2006). Erosion rates at the Mars exploration rover landing sites and long-term climate change on Mars. *Journal of Geophysical Research: Planets*, *111*(E12). doi: 10.1029/2006JE002754

Golombek, M. P., Warner, N. H., Ganti, V., Lamb, M. P., Parker, T. J., Fergason, R. L., & Sullivan, R. (2014). Small crater modification on meridiani planum and implications for erosion rates and climate change on Mars. *Journal of Geophysical Research: Planets*, *119*(12), 2522–2547. doi: 10.1002/2014JE004658

Goudge, T. A., Mohrig, D., Cardenas, B. T., Hughes, C. M., & Fassett, C. I. (2018, February). Stratigraphy and paleohydrology of delta channel deposits, jezero crater, Mars. *Icarus*, *301*, 58–75. Retrieved from `https://doi.org/10.1016/j.icarus.2017.09.034` doi: 10.1016/j.icarus.2017.09.034

Grotzinger, J., Arvidson, R., Bell, J., Calvin, W., Clark, B., Fike, D., ... Watters, W. (2005). Stratigraphy and sedimentology of a dry to wet eolian depositional system, Burns formation, Meridiani Planum, Mars. *Earth and Planetary Science Letters*, *240*(1), 11–72. doi: 10.1016/j.epsl.2005.09.039

Grotzinger, J. P., Crisp, J., Vasavada, A. R., Anderson, R. C., Baker, C. J., Barry, R., ... Wiens, R. C. (2012-09). Mars Science Laboratory Mission and Science Investigation. *Space Science Reviews*, *170*(1-4), 5–56. doi: 10.1007/s11214-012-9892-2

Grotzinger, J. P., Gupta, S., Malin, M. C., Rubin, D. M., Schieber, J., Siebach, K., ... Wilson, S. A. (2015, October). Deposition, exhumation, and paleoclimate of an ancient lake deposit, gale crater, Mars. *Science*, *350*(6257). doi: 10.1126/science.aac7575

Hajek, E. A., & Edmonds, D. A. (2014, March). Is river avulsion style controlled by floodplain

morphodynamics? *Geology*, *42*(3), 199–202. doi: 10.1130/G35045.1
Hajek, E. A., & Straub, K. M. (2017). Autogenic sedimentation in clastic stratigraphy. *Annual Review of Earth and Planetary Sciences*, *45*(1), 681-709. doi: 10.1146/annurev-earth-063016-015935
Hariharan, J., Passalacqua, P., Xu, Z., Michael, H. A., Steel, E., Chadwick, A., … Moodie, A. J. (2022). Modeling the dynamic response of river deltas to sea-level rise acceleration. *Journal of Geophysical Research: Earth Surface*, *127*(9). doi: 10.1029/2022JF006762
Hariharan, J., Wright, K., Moodie, A., Tull, N., & Passalacqua, P. (2023). Impacts of human modifications on material transport in deltas. *Earth Surface Dynamics*, *11*(3), 405–427. doi: 10.5194/esurf-11-405-2023
Hariharan, J., Xu, Z., Michael, H. A., Paola, C., Steel, E., & Passalacqua, P. (2021, August). Linking the surface and subsurface in river deltas—part 1: Relating surface and subsurface geometries. *Water Resources Research*, *57*(8). doi: 10.1029/2020wr029282
Hartmann, W. K. (1966). Martian cratering. *Icarus*, *5*(1), 565–576. doi: 10.1016/0019-1035(66)90071-6
Hartmann, W. K. (1971). Martian cratering iii: Theory of crater obliteration. *Icarus*, *15*(3), 410–428. doi: 10.1016/0019-1035(71)90119-9
Hartmann, W. K., & Neukum, G. (2001). Cratering chronology and the evolution of Mars. *Space Science Reviews*, *96*(1/4), 165–194. doi: 10.1023/a:1011945222010
Hayden, A. T., Lamb, M. P., Fischer, W. W., Ewing, R. C., McElroy, B. J., & Williams, R. M. (2019). Formation of sinuous ridges by inversion of river-channel belts in utah, usa, with implications for Mars. *Icarus*, *332*, 92–110. doi: 10.1016/j.icarus.2019.04.019
Herkenhoff, K. E., & Plaut, J. J. (2000). Surface ages and resurfacing rates of the polar layered deposits on Mars. *Icarus*, *144*(2), 243–253. doi: 10.1006/icar.1999.6287
Hiesinger, H., Head III, J. W., Wolf, U., Jaumann, R., & Neukum, G. (2002). Lunar mare basalt flow units: Thicknesses determined from crater size-frequency distributions. *Geophysical Research Letters*, *29*(8), 89-1–89-4. doi: 10.1029/2002GL014847
Hoke, M. R. T., & Hynek, B. M. (2009, August). Roaming zones of precipitation on ancient Mars as recorded in valley networks. *Journal of Geophysical Research: Planets*, *114*(E8). doi: 10.1029/2008je003247
Howard, A. (2004). Simple non-fluvial models of planetary surface modification, with application to Mars. In *Lunar and planetary science conference* (p. 1054).
Howard, A. D. (2007). Simulating the development of Martian highland landscapes through the interaction of impact cratering, fluvial erosion, and variable hydrologic forcing. *Geomorphology*, *91*(3), 332–363. doi: 10.1016/j.geomorph.2007.04.017
Irwin, R. P., Lewis, K. W., Howard, A. D., & Grant, J. A. (2015, July). Paleohydrology of eberswalde crater, Mars. *Geomorphology*, *240*, 83–101. Retrieved from `https://doi.org/10.1016/j.geomorph.2014.10.012` doi: 10.1016/j.geomorph.2014.10.012
Irwin, R. P., Tanaka, K. L., & Robbins, S. J. (2013, February). Distribution of early, middle, and late noachian cratered surfaces in the Martian highlands: Implications for resurfacing events and processes. *Journal of Geophysical Research: Planets*, *118*(2), 278–291. doi: 10.1002/jgre.20053
Ivanov, B. A. (2001). Mars/moon cratering rate ratio estimates. *Space Science Reviews*, *96*(1/4), 87–104. doi: 10.1023/a:1011941121102
Jerolmack, D. J., & Paola, C. (2007, November). Complexity in a cellular model of river avulsion. *Geomorphology*, *91*(3-4), 259–270. doi: 10.1016/j.geomorph.2007.04.022
Jerolmack, D. J., & Sadler, P. (2007). Transience and persistence in the depositional record of continental margins. *Journal of Geophysical Research: Earth Surface*, *112*(F3). doi: 10.1029/

2006JF000555

Kim, W., Petter, A., Straub, K., & Mohrig, D. (2014, August). Investigating the autogenic process response to allogenic forcing: experimental geomorphology and stratigraphy. In A. W. Martinius, R. Ravnås, J. A. Howell, R. J. Steel, & J. P. Wonham (Eds.), *From Depositional Systems to Sedimentary Successions on the Norwegian Continental Margin* (pp. 127–138). Chichester, UK: John Wiley & Sons, Ltd. doi: 10.1002/9781118920435.ch5

Kite, E. S. (2019, January). Geologic constraints on early Mars climate. *Space Science Reviews*, *215*(1). doi: 10.1007/s11214-018-0575-5

Kite, E. S., Lucas, A., & Fassett, C. I. (2013). Pacing early Mars river activity: Embedded craters in the aeolis dorsa region imply river activity spanned ≥(1–20)myr. *Icarus*, *225*(1), 850–855. doi: 10.1016/j.icarus.2013.03.029

Kite, E. S., Mischna, M. A., Fan, B., Morgan, A. M., Wilson, S. A., & Richardson, M. I. (2022, May). Changing spatial distribution of water flow charts major change in Mars's greenhouse effect. *Science Advances*, *8*(21). doi: 10.1126/sciadv.abo5894

Kite, E. S., Williams, J.-P., Lucas, A., & Aharonson, O. (2014, April). Low palaeopressure of the Martian atmosphere estimated from the size distribution of ancient craters. *Nature Geoscience*, *7*(5), 335–339. doi: 10.1038/ngeo2137

Lapôtre, M. G. A., & Ielpi, A. (2020). The pace of fluvial meanders on Mars and implications for the western delta deposits of jezero crater. *AGU Advances*, *1*(2). doi: 10.1029/2019AV000141

Lauzon, R., & Murray, A. B. (2018). Comparing the cohesive effects of mud and vegetation on delta evolution. *Geophysical Research Letters*, *45*(19), 10,437-10,445. doi: 10.1029/2018GL079405

Lauzon, R., Piliouras, A., & Rowland, J. C. (2019, June). Ice and permafrost effects on delta morphology and channel dynamics. *Geophysical Research Letters*. doi: 10.1029/2019GL082792

Leeder, M. (1978). A Quantitative Stratigraphic Model for Alluvium, with Special Reference to Channel Deposit Density and Interconnectedness. *Fluvial Sedimentology*, *Memoir 5*, 587–596.

Lewis, K. W., & Aharonson, O. (2014, June). Occurrence and origin of rhythmic sedimentary rocks on Mars. *Journal of Geophysical Research: Planets*, *119*(6), 1432–1457. doi: 10.1002/2013je004404

Liang, M., Geleynse, N., Edmonds, D. A., & Passalacqua, P. (2015b, January). A reduced-complexity model for river delta formation – Part 2: Assessment of the flow routing scheme. *Earth Surface Dynamics*, *3*(1), 87–104. doi: 10.5194/esurf-3-87-2015

Liang, M., Van Dyk, C., & Passalacqua, P. (2016, February). Quantifying the patterns and dynamics of river deltas under conditions of steady forcing and relative sea level rise: QUANTIFYING DELTA PATTERNS AND DYNAMICS. *Journal of Geophysical Research: Earth Surface*, *121*(2), 465–496. doi: 10.1002/2015JF003653

Liang, M., Voller, V. R., & Paola, C. (2015a, January). A reduced-complexity model for river delta formation – Part 1: Modeling deltas with channel dynamics. *Earth Surface Dynamics*, *3*(1), 67–86. doi: 10.5194/esurf-3-67-2015

Limaye, A. B. S., & Lamb, M. P. (2013). A vector-based method for bank-material tracking in coupled models of meandering and landscape evolution. *Journal of Geophysical Research: Earth Surface*, *118*(4), 2421–2437. doi: https://doi.org/10.1002/2013JF002854

Malin, M. C., & Edgett, K. S. (2000). Sedimentary rocks of early Mars. *Science*, *290*(5498), 1927–1937. doi: 10.1126/science.290.5498.1927

Mangold, N., Adeli, S., Conway, S., Ansan, V., & Langlais, B. (2012, April). A chronology of early Mars climatic evolution from impact crater degradation. *Journal of Geophysical Research: Planets*, *117*(E4). doi: 10.1029/2011je004005

Matsubara, Y., Howard, A. D., & Irwin, R. P. (2018, November). Constraints on the noachian paleoclimate of the Martian highlands from landscape evolution modeling. *Journal of Geophysical Research: Planets*, *123*(11), 2958–2979. doi: 10.1029/2018je005572

McEwen, A. S., Eliason, E. M., Bergstrom, J. W., Bridges, N. T., Hansen, C. J., Delamere, W. A., … Weitz, C. M. (2007). Mars reconnaissance orbiter's high resolution imaging science experiment (hirise). *Journal of Geophysical Research: Planets*, *112*(E5). doi: 10.1029/2005JE002605

Melosh, H. J. (1989). *Impact cratering : a geologic process*. New York, NY: Oxford University Press.

Michael, G. (2013). Planetary surface dating from crater size–frequency distribution measurements: Multiple resurfacing episodes and differential isochron fitting. *Icarus*, *226*(1), 885–890. doi: 10.1016/j.icarus.2013.07.004

Michael, G., Kneissl, T., & Neesemann, A. (2016). Planetary surface dating from crater size-frequency distribution measurements: Poisson timing analysis. *Icarus*, *277*, 279–285. doi: 10.1016/j.icarus.2016.05.019

Milliken, R. E., Grotzinger, J. P., & Thomson, B. J. (2010). Paleoclimate of Mars as captured by the stratigraphic record in gale crater. *Geophysical Research Letters*, *37*(4). doi: 10.1029/2009GL041870

Minton, D. A., Richardson, J. E., & Fassett, C. I. (2015). Re-examining the main asteroid belt as the primary source of ancient lunar craters. *Icarus*, *247*, 172–190. doi: 10.1016/j.icarus.2014.10.018

Mohrig, D., Heller, P. L., Paola, C., & Lyons, W. J. (2000). Interpreting avulsion process from ancient alluvial sequences: Guadalope-Matarranya system (northern Spain) and Wasatch Formation (western Colorado). *Geological Society of America Bulletin*, *112*(12), 1787–1803.

Moodie, A. J., Hariharan, J., Barefoot, E., & Passalacqua, P. (2021). pyDeltaRCM: a flexible numerical delta model. *Journal of Open Source Software*. doi: 10.21105/joss.03398

Moodie, A. J., Nittrouer, J. A., Ma, H., Carlson, B. N., Chadwick, A. J., Lamb, M. P., & Parker, G. (2019). Modeling deltaic lobe-building cycles and channel avulsions for the yellow river delta, china. *Journal of Geophysical Research: Earth Surface*, *124*(11), 2438–2462. doi: 10.1029/2019JF005220

Moodie, A. J., & Passalacqua, P. (2021). When does faulting-induced subsidence drive distributary network reorganization? *Geophysical Research Letters*, *48*(22). doi: 10.1029/2021GL095053

Neukum, G., & Horn, P. (1976). Effects of lava flows on lunar crater populations. *The Moon*, *15*(3-4), 205–222. doi: 10.1007/bf00562238

Öpik, E. J. (1966). The Martian surface. *Science*, *153*(3733), 255–265. doi: 10.1126/science.153.3733.255

Parker, G. (2004, November). *E-book: 1D sediment transport morphodynamics with applications to rivers and turbidity currents.* E-book. (Available at: http://hydrolab.illinois.edu/people/parkerg/morphodynamics_e-book.htm)

Parker, G., Paola, C., Whipple, K. X., Mohrig, D., Toro-Escobar, C. M., Halverson, M., & Skoglund, T. W. (1998, October). Alluvial Fans Formed by Channelized Fluvial and Sheet Flow. II: Application. *Journal of Hydraulic Engineering*, *124*(10), 996–1004. doi: 10.1061/(ASCE)0733-9429(1998)124:10(996)

Pike, R. J. (1977, January). Size-dependence in the shape of fresh impact craters on the moon. In D. J. Roddy, R. O. Pepin, & R. B. Merrill (Eds.), *Impact and explosion cratering: Planetary and terrestrial implications* (pp. 489–509).

Piliouras, A., Lauzon, R., & Rowland, J. C. (2021). Unraveling the combined effects of ice and permafrost on arctic delta morphodynamics. *Journal of Geophysical Research: Earth Surface*, *126*(4). doi: 10.1029/2020JF005706

Popova, O., Nemtchinov, I., & Hartmann, W. K. (2003, June). Bolides in the present and past Martian atmosphere and effects on cratering processes. *Meteoritics & Planetary Science*, *38*(6), 905–925. doi: 10.1111/j.1945-5100.2003.tb00287.x

Reitz, M. D., & Jerolmack, D. J. (2012, May). Experimental alluvial fan evolution: Channel dynamics, slope controls, and shoreline growth. *Journal of Geophysical Research*, *117*(F2). doi: 10.1029/2011JF002261

Reitz, M. D., Jerolmack, D. J., & Swenson, J. B. (2010, March). Flooding and flow path selection on alluvial fans and deltas: FLOW PATH SELECTION ON ALLUVIAL FANS. *Geophysical Research Letters*, *37*(6), n/a–n/a. doi: 10.1029/2009GL041985

Richardson, J. E. (2009). Cratering saturation and equilibrium: A new model looks at an old problem. *Icarus*, *204*(2), 697–715. doi: 10.1016/j.icarus.2009.07.029

Richardson, J. E., Melosh, H. J., & Greenberg, R. (2004). Impact-induced seismic activity on asteroid 433 eros: A surface modification process. *Science*, *306*(5701), 1526–1529. doi: 10.1126/science.1104731

Richardson, J. E., Melosh, H. J., Greenberg, R. J., & O'Brien, D. P. (2005). The global effects of impact-induced seismic activity on fractured asteroid surface morphology. *Icarus*, *179*(2), 325–349. doi: 10.1016/j.icarus.2005.07.005

Robbins, S. J., & Hynek, B. M. (2012). A new global database of Mars impact craters $\geq$1 km: 2. global crater properties and regional variations of the simple-to-complex transition diameter. *Journal of Geophysical Research: Planets*, *117*(E6). doi: 10.1029/2011JE003967

Ross, H. P. (1968). A simplified mathematical model for lunar crater erosion. *Journal of Geophysical Research (1896-1977)*, *73*(4), 1343–1354. doi: 10.1029/JB073i004p01343

Russ, J. C. (1986). *Practical stereology*. Springer US. doi: 10.1007/978-1-4899-3533-5

Sadler, P. M. (1981). Sediment accumulation rates and the completeness of stratigraphic sections. *The Journal of Geology*, *89*(5), 569–584. doi: 10.1086/628623

Schultz, P. H., & Gault, D. E. (1975, January). Seismically induced modification of lunar surface features. *Lunar and Planetary Science Conference Proceedings*, *3*, 2845–2862.

Schumer, R., Jerolmack, D., & McElroy, B. (2011). The stratigraphic filter and bias in measurement of geologic rates. *Geophysical Research Letters*, *38*(11). doi: 10.1029/2011GL047118

Schumm, S. A. (1985). Patterns of alluvial rivers. *Annual Review of Earth and Planetary Sciences*, *13*(1), 5–27. doi: 10.1146/annurev.ea.13.050185.000253

Shannon, C. (1949). Communication in the Presence of Noise. *Proceedings of the IRE*, *37*(1), 10–21. doi: 10.1109/JRPROC.1949.232969

Slingerland, R., & Smith, N. D. (2004, May). RIVER AVULSIONS AND THEIR DEPOSITS. *Annual Review of Earth and Planetary Sciences*, *32*(1), 257–285. doi: 10.1146/annurev.earth.32.101802.120201

Smith, M. R., Gillespie, A. R., & Montgomery, D. R. (2008). Effect of obliteration on crater-count chronologies for Martian surfaces. *Geophysical Research Letters*, *35*(10). doi: 10.1029/2008GL033538

Smith, N. D., Cross, T. A., Dufficy, J. P., & Clough, S. R. (1989, February). Anatomy of an avulsion. *Sedimentology*, *36*(1), 1–23. doi: 10.1111/j.1365-3091.1989.tb00817.x

Soderblom, L. A. (1970). A model for small-impact erosion applied to the lunar surface. *Journal of Geophysical Research (1896-1977)*, *75*(14), 2655–2661. doi: 10.1029/JB075i014p02655

Stack-Morgan, K. M., Gupta, S., Tebolt, M., Caravaca, G., Ives, L. R., Russell, P., … Williams, R. M. (2023). Sedimentology and stratigraphy of the lower delta sequence, jezero crater, Mars. The Woodlands, TX, USA.

Straub, K. M., Duller, R. A., Foreman, B. Z., & Hajek, E. A. (2020). Buffered, incomplete, and shredded: The challenges of reading an imperfect stratigraphic record. *Journal of Geophysical Research: Earth Surface*, *125*(3). doi: 10.1029/2019JF005079

Straub, K. M., & Esposito, C. R. (2013). Influence of water and sediment supply on the stratigraphic record of alluvial fans and deltas: Process controls on stratigraphic completeness. *Journal of Geophysical Research: Earth Surface*, *118*(2), 625-637. doi: 10.1002/jgrf.20061

Straub, K. M., Li, Q., & Benson, W. M. (2015). Influence of sediment cohesion on deltaic shoreline dynamics and bulk sediment retention: A laboratory study. *Geophysical Research Letters*, *42*(22), 9808–9815. doi: 10.1002/2015GL066131

Straub, K. M., Paola, C., Mohrig, D., Wolinsky, M. A., & George, T. (2009, 09). Compensational Stacking of Channelized Sedimentary Deposits. *Journal of Sedimentary Research*, *79*(9), 673-688. doi: 10.2110/jsr.2009.070

Stucky de Quay, G., Goudge, T. A., Kite, E. S., Fassett, C. I., & Guzewich, S. D. (2021, August). Limits on runoff episode duration for early Mars: Integrating lake hydrology and climate models. *Geophysical Research Letters*, *48*(15). doi: 10.1029/2021gl093523

Tejedor, A., Schwenk, J., Kleinhans, M., Limaye, A. B., Vulis, L., Carling, P., . . . Foufoula-Georgiou, E. (2022, August). The entropic braiding index (ebi): A robust metric to account for the diversity of channel scales in multi-thread rivers. *Geophysical Research Letters*, *49*(16). doi: 10.1029/2022gl099681

Trampush, S. M., Huzurbazar, S., & McElroy, B. (2014). Empirical assessment of theory for bankfull characteristics of alluvial channels. *Water Resources Research*, *50*(12), 9211-9220. doi: 10.1002/2014WR015597

Vasavada, A. R. (2022). Mission Overview and Scientific Contributions from the Mars Science Laboratory Curiosity Rover After Eight Years of Surface Operations. *Space Science Reviews*, *218*(3), 14. doi: 10.1007/s11214-022-00882-7

Wang, Y., Straub, K. M., & Hajek, E. A. (2011). Scale-dependent compensational stacking: An estimate of autogenic time scales in channelized sedimentary deposits. *Geology*, *39*(9), 811–814. doi: 10.1130/G32068.1

Warren, A. O., Kite, E. S., Williams, J.-P., & Horgan, B. (2019). Through the thick and thin: New constraints on Mars paleopressure history 3.8–4 ga from small exhumed craters. *Journal of Geophysical Research: Planets*, *124*(11), 2793–2818. doi: 10.1029/2019JE006178

Wells, N. A., & Dorr, J. A. (1987). Shifting of the Kosi River, northern India. *Geology*, *15*(3), 204. doi: 10.1130/0091-7613(1987)15$⟨$204:SOTKRN$⟩$2.0.CO;2

Wickert, A. D., Martin, J. M., Tal, M., Kim, W., Sheets, B., & Paola, C. (2013, June). River channel lateral mobility: metrics, time scales, and controls: RIVER CHANNEL LATERAL MOBILITY. *Journal of Geophysical Research: Earth Surface*, *118*(2), 396–412. doi: 10.1029/2012JF002386

Williams, J.-P., Pathare, A. V., & Aharonson, O. (2014). The production of small primary craters on Mars and the moon. *Icarus*, *235*, 23–36. doi: 10.1016/j.icarus.2014.03.011

Williams, J.-P., van der Bogert, C. H., Pathare, A. V., Michael, G. G., Kirchoff, M. R., & Hiesinger, H. (2018). Dating very young planetary surfaces from crater statistics: A review of issues and challenges. *Meteoritics & Planetary Science*, *53*(4), 554–582. doi: 10.1111/maps.12924

Wolman, M. G., & Miller, J. P. (1960, January). Magnitude and Frequency of Forces in Geomorphic Processes. *The Journal of Geology*, *68*(1), 54–74. doi: 10.1086/626637

Woronow, A. (1977). Crater saturation and equilibrium: A monte carlo simulation. *Journal of Geophysical Research (1896-1977)*, *82*(17), 2447–2456. doi: 10.1029/JB082i017p02447

Woronow, A. (1978). A general cratering-history model and its implications for the lunar highlands. *Icarus*, *34*(1), 76–88. doi: 10.1016/0019-1035(78)90127-6

Wright, K., Hariharan, J., Passalacqua, P., Salter, G., & Lamb, M. P. (2022). From grains to plastics: Modeling nourishment patterns and hydraulic sorting of fluvially transported materials in deltas. *Journal of Geophysical Research: Earth Surface*, *127*(11), e2022JF006769. doi: 10.1029/2022JF006769

Yielding, G., Needham, T., & Jones, H. (1996). Sampling of fault populations using sub-surface data: a review. *Journal of Structural Geology*, *18*(2), 135–146. doi: 10.1016/S0191-8141(96)80039-3

Supporting Information for:
Fluvial reworking eliminates small craters, but does not meaningfully bias the Mars interbedded-crater record

Andrew J. Moodie[1,2] and Timothy A. Goudge[2,3]

[1]Department of Geography, Texas A&M University

[2]Department of Earth and Planetary Sciences, The University of Texas at Austin

[3]Center for Planetary Systems Habitability, The University of Texas at Austin

Contents of this file

S1. Additional information on the numerical model and modeling choices

The only direct use of the gravitational acceleration constant (g, m/s^2) in the DeltaRCM delta model is through influencing a weighting parameter (γ) that plays a role in water routing. γ partitions the importance of the water surface gradient and flow inertia in setting the "average downstream direction of flow" through a cell $\boldsymbol{F}$ as:

$$\boldsymbol{F}* = \gamma \boldsymbol{F}_{sfc} + (1-\gamma)\boldsymbol{F}_{int} \quad \text{and} \quad \boldsymbol{F} = \frac{\boldsymbol{F}*}{|\boldsymbol{F}*|}, \tag{S1}$$

where $\boldsymbol{F}_{sfc}$ and $\boldsymbol{F}_{int}$ are unit vectors calculated from the water surface gradient and water discharge field (i.e., inertia), respectively. In the original DeltaRCM model code published alongside Liang, Voller, and Paola (2015a), γ is determined as:

$$\gamma = \frac{gS\Delta x}{u^2}, \tag{S2}$$

where S and u are the the inlet channel slope and flow velocity, respectively, and Δx is the model domain grid spacing.

The downstream direction unit vector $\boldsymbol{F}$ is then used to determine the probability of a water parcel being routed to one of eight neighboring cells, according to the expression:

$$w_i = \frac{h_i \max(0, \boldsymbol{F}\cdot \boldsymbol{d}_i)}{\Delta_i}, \tag{S3}$$

where h_i is depth, $\boldsymbol{d}_i$ is the cellular direction vector pointing to neighbor i from the given cell, and Δ_i is the cellular distance: 1 for cells in main compass directions and $\sqrt{2}$ for corner cell (Liang et al., 2015a). Thus, the weighted random walk of water parcels through the domain depends principally on bed topography and flow inertia: a relatively flat local water surface means variations in flow depth h_i arise from bed topography, and the typically small value of γ means that $\boldsymbol{F}$ is mostly controlled by the inertial term. In gross, deeper cells in approximately the average flow direction are more likely to be stepped into during the weighted random walk of water parcels (Liang et al., 2015a).

We elected not to modify these aspects of the model for our study, including not modifying the gravitational acceleration constant from -9.81 m/s^2 (i.e., an average value on Earth). We chose not to modify g because we do not want to misrepresent our simulations as representing the differences between river and delta processes on Earth and Mars. DeltaRCM is a rules-based reduced-complexity model that relies on physical intuition and theory to define algorithms and parameterize rules, and therefore does not parametrically link all functions that conceptually depend on gravity to the gravitational constant.

To reiterate, there are additional model parameters (other than γ) that *conceptually* relate to gravitational acceleration, but can not be directly controlled in the present model because these additional parameters do not have physics-based formulas that include the gravitational acceleration constant g. For example, the relationship between gravity and sediment transport rates is known to be important to delta growth (Braat et al., 2021), but DeltaRCM is not formulated to make this connection; making this connection would require a specification of grain size in the model that does not currently exist. There are several other relationships that would need to be established (i.e., physics-based formulas for parameters) to make gravitational acceleration a directly tunable parameter in the model (Braat et al., 2024). This research and development is an interesting direction for future research, but is beyond the scope of this study.

Although we do not believe changing γ in the model to be fully representative of the effect of changing gravity on fluvial deltaic processes, we ran several simulations to demonstrate that our study results are not sensitive to the choice in γ. In fact, we can hypothesize this insensitivity to γ given the structure of Equations S1–S3: changing the gravitational constant has a diminished impact on local routing weights (Equation S3) once topography is established and water depths (h) vary locally. For example, for the model domain configuration used in the main text, when g = 9.81 m/s^2 (Earth) the balancing parameter γ = 0.0131, and for g = 3.71 m/s^2 (Mars) the balancing parameter γ = 0.0049. This difference means that $\boldsymbol{F}*$ is either 98.7% dependent (Earth) on the water discharge field (i.e., inertia), or 99.5% dependent (Mars) on the water discharge field, with the remainder due to the water surface gradient. Moreover, this factor of three change in γ does not directly modify the local routing weights (Equation S3); instead, the unit vector $\boldsymbol{F}$ is combined with a downstream-average directed unit vector, and with local water depths to determine local routing weights (Equation S3). In the end, because water depths vary on the order of 10^1, whereas $\boldsymbol{F} \cdot d$ is always < 1 (i.e., varies on the order 10^0) local routing weights are more influenced by flow depth than γ, regardless of the value of gamma. We test this theory on the role of γ below.

A notable exception to the theory described above is during the early stages of delta formation, when the receiving basin is empty with a flat bed, and thus water depth and the water surface elevation are approximately equal everywhere. As a result, the flow inertia is the dominant property influencing water routing weights in these early model stages (Equations S1–S3). The resulting difference in delta morphology from a factor of three change in γ (as derived from a factor of three change in gravity between Earth and Mars) is shown in the supplementary material of the original DeltaRCM paper (Liang et al., 2015a). This numerical experiment runs delta building over a relatively short timescale, such that most of the simulation is consistent with the early-stage flow routing inertia-dominated regime. We believe the difference in model results shown in that experiment will be diminished in longer-running simulations.

To test this, we ran six simulations with the same configuration as the primary experiments in the main text (i.e,. same domain size, grid cell size, basin depth, inlet flow velocity, simulation duration, etc.), but varying sand fraction and gravitational acceleration constant g. These simulations varied the input sand fraction in line with the main text simulations (0.2, 0.5, and 0.8 sand fraction), and varied the gravitational acceleration constant as g = 9.81 m/s^2 (Earth) and g = 3.71 m/s^2 (Mars); this results in values of γ = 0.0131 and γ = 0.0049 for Earth and Mars gravity, respectively. The final configuration of the river-delta system for each simulation is shown in Figure S1.

Visual inspection of Figure S1 indicates that the change in the fluvial-deltaic deposit as a result of change in the sand fraction parameter is greater than the difference due to change in gravitational acceleration constant (and therefore change in γ). Qualitatively, the lower-γ simulations appear to be more lobate, with this difference most apparent in the sandy ($f = 0.8$) simulations; this result is consistent with the expectation that a lower γ increases the role of inertia in routing water through the domain (Liang et al., 2015a).

This sensitivity test supports our decision to not vary the gravitational acceleration constant: in this model, this parameter alone does not have a pronounced effect. A recent study demonstrates how sediment suspensions and therefore total sediment transport may be enhanced under reduced Mars gravity (Braat et al., 2024), but gravity does not impact sediment suspension or transport in the DeltaRCM model. It may be possible to modify routing rules for sand and mud in the DeltaRCM framework to represent this enhanced suspension; for example, following interpretations of the θ parameter as a proxy for vertical material stratification (Hariharan et al., 2020; Wright et al., 2022). This is an interesting subject for future research.

S2. Crater preservation metrics in detail

We performed additional analyses and metric calculations of crater reworking that were not included in the main text (Figure S2). Overall, these additional analyses confirm that the model is working as expected, and that study conclusions cannot be attributed to another process.

We first compared the diameter of craters determined as interbedded versus those not identified as being interbedded (Figure S2a), to validate that our automatic labeling of interbedded craters was not imparting any size-dependent bias on the crater record. We identify no difference between the diameters of the interbedded craters and non-interbedded craters; or specifically, we cannot reject the null hypothesis that the distributions are from the same population in a two-sample t-test (p=0.68). Subsequent analyses and figures in this section include only interbedded craters.

Next, we assess the potential for a time bias to explain observations of crater preservation, in essence, testing alternative hypothesis that preservation is controlled mostly by the time a crater was formed and more recently formed craters will be better preserved; note that time here is cast as elapsed model seconds, which according to the model intermittency formulation scales linearly to the 1, 10, and 100 Myr crater accumulation timescales. Figure S2b shows that there a slight tendency for the very oldest craters to be less preserved than craters throughout the rest of the simulation. But, in gross, there is not a clear relationship between crater rim fraction preserved and model simulation time We additionally investigated whether a time-based preservation bias existed in the data at all by considering only preservation at the delta landform surface at the end of simulation (Figure S2c). Indeed, older craters are less preserved at the delta surface; this is indicative of both burial by sediment over time (i.e., preservation in stratigraphy) and fluvial reworking of sediments at the surface. Interestingly, comparing rim fraction preserved at the sediment surface to crater diameter (Figure S2d) reveals a pattern similar to the overall preservation metric from the main text (Figure 5a). Together, these patterns suggest that the model and analyses are working as expected: creating interbedded craters that are either buried or reworked (or both) over time.

Another facet of the data to examine was whether crater position on the delta affected preservation. Figure S2e shows that the distance from the inlet channel a crater formed has no influence on the preservation of that crater. Consistent with the notion of a deltaic landform that grows over time, there is a (noisy) decrease in age of craters with increasing distance from the inlet (apparent from the broad purple-to-green-to-yellow shift from left to right in Figure S2e).

We examined whether there was any trend in preservation as it related to the elevation of the sediment surface (i.e., the land or bottom of shallow sea) upon which the crater formed (Figure S2f); this elevation is termed the reference elevation (Howard, 2007). Here, the data also record the expected pattern of a delta growing over time, with higher reference elevations occurring only later in elapsed model time. Importantly though, there is no discernible relationship between reference elevation and rim fraction preserved (Figure S2f), indicating that this is not a factor biasing interbedded crater size-frequency distributions.

To understand the correlation we between rim fraction preserved and preserved rim continuity, we examined how these metrics compared for each interbedded crater (Figure S2g). As expected, metrics are clearly correlated, though the rim fraction preserved is (with very few exceptions) higher than the commensurate preserved rim continuity, on a normalized basis (e.g., 0.5 commensurate with 180°). This asymmetry arises because preserved rim continuity is a more strict metric, in the sense that narrow breaks in rim continuity immediately lower the metric, but fraction preserved can still be high.

Finally, we display the timeseries of crater sizes (aggregated across all simulations to demonstrate that cratering is treated as a Poisson process, with arrival times (i.e., crater production times) independent of all other events (Figure S2h).

S3. Cumulative distribution sensitivities

We examined the sensitivity of crater-size cumulative distributions to various steps in our workflow. Figure S3 shows how fluvial reworking-biased distributions, as well as distributions biased by fluvial reworking and exhumation, vary when extracted for a single simulation with duration 1, 10, or 100 Myr, and are characterized by a smaller number of craters (11 craters, rather than 56). To generate these distributions (Figure S3), we randomly selected a single simulation from each simulation-duration ensemble, then followed the same analysis routine as in the main text. In short, to characterize fluvial reworking bias, we first randomly select 11 interbedded craters from the simulation, then exclude those craters with <180° rim continuity, and repeat this process 100 times to assess distribution variability; we show the median distribution as a solid line, and 16th to 84th percentile distributions as a shaded envelope. We then characterize exhumation bias by applying an increased weighting probability for larger craters to be sampled, whereby probability of a crater with diameter d to be included in the synthetic distribution goes as $p(d) \propto d/d_{min}$, where d_{min} ≈10 m is the smallest crater diameter in the simulations.

With the exception of the 1 Myr duration simulation (Figure S3a), cumulative distributions generated for individual simulations are similar to the aggregated simulation results (Figure 6). In the 1 Myr case (Figure S3a), the crater size distribution is narrow and ranges 10–30 m diameter craters, such that the sampled distributions deviate from the distribution of all interbedded craters. In the 10 Myr case (Figure S3b), fluvial reworking leads to enhanced bias and increased variability with respect to the aggregated simulation results (Figure 6), though the median distribution does not scale similarly to observed crater size-frequency distributions on Mars. In the 100 Myr case (Figure S3c), the results are effectively identical to the aggregated simulation results (i.e., Figure 6), but with a larger amount of variability here that arises due to the small sample size (11 craters sampled, rather than 56). The total number of interbedded craters in a single 1 Myr duration simulation (10–33) is substantially fewer than a 100 Myr duration simulation (1625–2894), such that cumulative distributions generated from a single 1 Myr duration simulation are especially susceptible to small number effects. Importantly, even in the extreme cases of small number statistics demonstrated here, no sampled distributions reproduce observed crater size-frequency distributions on Mars.

Additionally, we examined how cumulative distributions made from the aggregated simulation results are modulated by the selected rim continuity threshold, the number of craters observed in the crater record, and exhumational bias (Figure S4). In this part of the sensitivity analysis, we follow the same workflow as in the main text but isolated one component of the workflow to vary, and calculated *only the combined effect* of fluvial reworking and exhumational bias for visual clarity in figures; all figures show the median distribution as a solid line, and 16th to 84th percentile distributions as a shaded envelope.

In the main text, we use a rim continuity threshold of 180° to determine which interbedded craters are mappable, so we varied this threshold from 60° to 310° here (Figure S4a). There is some variation in median distributions, but the envelope of variability in the distributions is overlapping, leading us to conclude there is little difference in the outcome of our study with selection of a different rim continuity threshold. Though we do not robustly validate this idea, we suspect that the limited variability arises from the fact that distributions are dominated by smaller craters ($\leq$50 m) that are less than a channel width in diameter, and so are often either completely removed or completely preserved, and therefore contribute equally cumulative distributions when the rim continuity threshold is varied 60°–310°. Additionally, spatial discretization of crater deposits creates discrete quanta for preservation metrics of smaller craters, because there are only 8 cells that make up the crater rim (see main text and Section 5); this also potentially limits the impact of the selected rim continuity threshold.

In the main text, we use 56 craters from the interbedded crater record to generate cumulative distribution functions and compare with the Mars crater record (i.e., Figure 6), so varied the number of craters selected in generating cumulative distributions from 24 to 88 here (Figure S4b). Distribution medians and envelopes of variability are indistinguishable from one another, indicating that this choice has little effect on results. Note that, when selecting only 11 craters from a single 1 Myr simulation (Figure S3a) it is possible to modulate crater size cumulative distributions. However, for values that can reasonably be considered representative samples (n=24 to 88; Figure S4b), the number of samples does not affect the interpretation that fluvial reworking and exhumation bias cannot explain the observed record.

In the main text, we represent exhumation bias as an increased observation probability based on crater diameter. We attempted to validate the theory underlying this proportional scaling in the course of our research, and determined that it likely provides an acceptable first-order approximation of the effect; we discuss this empirical validation, and opportunities for further research briefly in the main text (Section 4.4.3), and in more detail below in Section 6. Here, we demonstrate possible distributions that could be generated by various proportionalities of exhumational bias. We selected exponents l from 0.5 to 2.5, that modify the proportionality as $p(d) \propto d^l/d_{min}$ (Figure S4c); $l = 1$ is the default proportionality and is used throughout the main text. Exhumational bias has the largest impact on CSFDs of all threshold sensitivities examined. But, even in the most extreme case of $l = 2.5$, exhumational bias cannot reproduce observed crater records. Notably, in our empirical testing of exhumational bias, we determined that an exhumational bias proportional to the diameter squared (d^2) yields an exponent k of -1.2, consistent with the bias of smallest craters observed in the slow aggradation simulation. It is not clear to us whether increased exhumational bias (e.g., ($\propto d^2$) in combination with fluvial reworking and other uncertain degradation processes, might meaningfully modulate cumulative crater size distributions. This will be an important area for future research, and could be achieved with a landscape evolution model simulating erosional exhumation of craters embedded in heterogeneous sedimentary volumes (e.g., Cardenas et al., 2022).

S4. Effect of crater obliteration on metrics and conclusions

We quantified the effect of crater obliteration, that is, the destruction of an existing crater when a new crater is formed, on metrics used in our analyses. This process is implicitly included in our simulations, and we want to understand the magnitude of crater removal due to obliteration, relative to fluvial reworking. To quantify the effect, we ran nine simulations without river-delta sediment input, and generated craters according to the same routine as the main text. In these sensitivity test simulations, the synthesized crater size-frequency distribution was consistent with the Ivanov (2001) production function, and the Hartmann and Neukum (2001) Mars chronology function for 100 Myr of elapsed time beginning 3.5 Ga (e.g., Figure 2).

We calculated the rim fraction preserved, ejecta fraction preserved, and preserved rim continuity in the same way as the main text (Figure S5). It is well known that crater obliteration leads to a size-dependent bias that preferentially eliminates smaller craters from the crater record (Woronow, 1977, 1978; Smith et al., 2008; Richardson, 2009; Minton et al., 2015). Our sensitivity testing reveals the same observation, with all three crater preservation metrics showing a preferential removal of smaller craters (Figure S5). Notably, 25 m-bin averages indicate that the average effect of crater obliteration is smaller than the fluvial reworking effect (i.e., Figure 5). Importantly, this sensitivity test is an overestimate of the magnitude of the crater obliteration effect in the main text simulations. In main text simulations, craters can be incorporated into the stratigraphic record over time, and therefore move away fro the sediment surface and are less susceptible to overprinting by subsequent craters.

S5. Space and time discretization effects

Our model and analysis are executed on a rectilinear grid, which leads to spatial and temporal discretization effects. Spatial discretization effects are introduced to our workflow at two critical points: first, when craters are created on the model grid, and second when we convert a model elevation timeseries to a stratigraphic volume. Temporal discretization is introduced into our workflow during model simulation, because model state is only intermittently recorded (not continuously). Here, we consider the potential impact of these effects on our results. Importantly, we determine that study conclusions are not affected by spatial and temporal discretization, though precise values of reworking may be sensitive to vertical discretization.

Figure S6a shows the spatially discretized topography along a transect through the center of craters with varying diameters. Although crater depressions consistently become wider with increasing diameter, the maximum height does not monotonically increase due to discretization. Note, that this effect is fairly minor (a few meters difference for a 60 versus 80 m diameter crater), and that there is an overall trend of increasing maximum rim height

Discretized rim height is less than analytical rim height for modeled crater sizes $\lesssim$ 100 m, and drops to a constant value of 0.2 m for craters $<$ 10 m in diameter (Figure S6b). For these smallest crater diameters, the distance from crater center to rim is less than one half grid cell width, so the rim is not effectively rendered on the grid; this discretization is related to a Nyquist-Shannon wavelength (Shannon, 1949). At crater sizes ¡40 m, the maximum height of craters discretized to the model grid is less than height determined by the Howard 2007 analytical expressions and less than the 4% rim-height approximation (Robbins et al., 2012). At the small end of the crater-size range of interest, craters 10 m in diameter have an initial rim height of 5 m according to the Howard 2007 expression and 40 cm according to the 4% approximation, and the discretized rim height in our model for a 10 m diameter crater is $\sim$10 cm (Figure R1). The deviation between discretized and theoretical fresh-crater rim geometry diminishes to 0% for craters 40 m in diameter (Figure S6). Both the Howard expression and 4% approximation are based on craters $\geq$1 km in diameter (and are both approximations), and we are not aware of a scaling relationship specifically for smaller craters. In any case, rims of craters in this diameter range likely present very little vertical obstruction to flow conveyed in channels that average 7$\pm$3 m in depth. Thus, discretization could lead to a small overestimate of reworking of the smallest fraction of crater sizes in our study, but we do not expect this could explain or meaningfully impact the overall trends and conclusions of our study. We did not examine the effect of vertical or horizontal spatial discretization in detail for this article.

Temporal discretization arises because not every iteration of the numerical delta model is written to file. Therefore, there is potential that crater rims and ejecta are reworked by either fluvial processes or by obliteration during formation of new craters. In any case, the potential bias from temporal discretization is minimized by saving model state to the output file frequently (Hariharan et al., 2021). We quantified the effect of crater obliteration through a record of craters representing 100 Myr elapsed time, and the effect is relatively minor as compared to fluvial reworking (Section 4). Channels occupy a small fraction of the overall delta area at any point in time, so it seems unlikely a large number of craters would be reworked before recorded. Given these facts, we do not expect that temporal discretization has any impact on trends and conclusions identified in our study.

S6. Exhumation bias proportionality

Exhumational bias is the interacting set of processes that preferentially expose larger craters when a sedimentary volume with interbedded craters is eroded (Kite et al., 2013). Stereological theory underpins exhumational bias (Russ, 1986; Yielding et al., 1996); in short, the likelihood of a plane through a three-dimensional volume intersecting an object embedded in the volume depends on the object length-scale in the axis normal to the plane. For an erosional surface that cuts a quasi-horizontal plane through a sedimentary volume with embedded craters, the likelihood a crater is exposed on the plane therefore depends on the crater depth. Assuming a semi-hemispherical crater shape fixes the ratio between crater diameter and depth (e.g., Melosh, 1989), and therefore makes exhumational probability proportional to crater diameter (Kite et al., 2014; Warren et al., 2019; Lewis & Aharonson, 2014). However, this framework assumes that 1) the largest crater depths are small with respect to the sedimentary volume thickness, 2) that erosional surfaces are reasonably approximated by planes, and 3) that proportionality of exhuming crater deposits (i.e., rim and ejecta material) is the same as the probability of exhuming the bowl-like depression of a crater. Our study accepted these assumptions, but sensitivity testing indicates that further scrutiny of this geometry-based exhumational bias model is needed.

We attempted to empirically validate the exhumational bias relevant to our study (i.e., exhumed crater rim deposits), by modeling crater rim and ejecta deposits randomly embedded in a stratigraphic volume and subsequently exhumed along a horizontal plane. To do so, we created a set of model runs with the same parameterizations as 100 Myr simulations, but with a broader range of craters generated ranging 10–1000 m in diameter, and with sediment accumulation set to be constant and uniform over the model domain; in essence, we turn off fluvial-deltaic sedimentation and impose burial at a specified vertical rate. We examined the effect of a fast (1 m/Myr) and a slow (0.06 m/Myr) sediment accumulation rate, which correspond to sediment thicknesses of 100 m and 6 m, respectively; 6 m is approximately the thickness of deposits modeled in this study. After simulation, we randomly selected 51 horizontal planes from the stratigraphic volume, and identified crater rim deposits that intersected with the plane (emphasis: only crater rim deposits were counted), and repeated this analysis on a second replicate simulation for each of fast and slow aggradation. Similar to analysis in our study, this routine assumes that exhumation does not degrade craters, but only exposes or completely eliminates them from the record, and is affected by crater obliteration during formation of new craters (like simulations in the main text). Finally, we fit an exponent *k* to the recovered crater size-frequency distributions consistent with an imposed power-law CSFD (e.g., Hartmann, 2005).

These tests indicate that a sampling probability proportional to crater diameter is a conservative (i.e., lower-bound) estimate of the exhumational bias effect (Figure S7). The exponent fit to the full crater size-frequency distribution is -3, which is consistent with the expectation from crater production functions (Hartmann, 2005). When sampling proportional to diameter (i.e., exactly as we do in the main text), we find the fit exponent is -2, which is consistent with the theory (Lewis & Aharonson, 2014). When empirically sampling the idealized sedimentary volumes via intersection with random horizontal planes, we find the fit exponent is -1.6 and -1.2 for the fast and slow aggradation volumes, respectively. That is, sampling bias is more extreme in both empirical tests than in proportional sampling, and potentially largest in slow-aggradation environments.

In the fast aggradation case where the sedimentary volume reaches 100 m in thickness, the best-fit exponent of the power law appears to reasonably explain the individual observed sets of craters (Figure S7). This is in contrast to the trend between individual sets of craters empirically sampled from the slow aggradation case, and the best-fit exponent. Looking in detail at the slow aggradation case, the sampled distributions follow closely with the full crater size-frequency distribution for crater diameters $\gtrsim 40$ m, and diverge considerably over smaller crater diameters (Figure S7). That is, larger crater rim deposits are *nearly always* sampled by exhumation bias when the deposit thickness is low, but there is only a chance that smaller crater rim deposits are sampled thereby imparting a bias. The best-fit coefficient may therefore be erroneous for this slow-aggradation case, but bias among smaller craters is consistent with the faster aggradation case and different from the probabilistic exhumation (i.e., > -2).

We note that in empirical sampling, we tested for intersection with crater rim deposits and not the bowl-like depression of a crater. There is no easy way to test for the latter in our modeling approach, so we did not separate the effect on the exponent of what is intersected and aggradation rate. Though, if aggradation rate did not also have some effect, there would be no difference between fast and slow tests.

In sum, we do not expect that even the most extreme plausible exhumation bias determined by these experiments would favor larger craters so significantly that our results would change. It will be an interesting topic for future modeling studies to explore how crater deposits are morphodynamically exhumed from sedimentary strata, and therefore examine exhumational bias in greater detail.

References

Braat, L., Brückner, M. Z. M., Sefton-Nash, E., & Lamb, M. P. (2024). Gravity-driven differences in fluvial sediment transport on mars and earth. *Journal of Geophysical Research: Planets*, *129*(2). doi: 10.1029/2023JE007788

Braat, L., Lamb, M., & Sefton-Nash, E. (2021). Differences between deltas on earth and mars.. Retrieved from `https://essopenarchive.org/doi/full/10.1002/essoar.10509327.1` doi: 10.1002/essoar.10509327.1

Cardenas, B. T., Lamb, M. P., & Grotzinger, J. P. (2022, October). Martian landscapes of fluvial ridges carved from ancient sedimentary basin fill. *Nature Geoscience*, *15*(11), 871–877. doi: 10.1038/s41561-022-01058-2

Hariharan, J., Wright, K., & Passalacqua, P. (2020, October). dorado: A python package for simulating passive particle transport in shallow-water flows. *Journal of Open Source Software*, *5*(54), 2585. doi: 10.21105/joss.02585

Hariharan, J., Xu, Z., Michael, H. A., Paola, C., Steel, E., & Passalacqua, P. (2021, August). Linking the surface and subsurface in river deltas—part 1: Relating surface and subsurface geometries. *Water Resources Research*, *57*(8). doi: 10.1029/2020wr029282

Hartmann, W. K. (2005). Martian cratering 8: Isochron refinement and the chronology of Mars. *Icarus*, *174*(2), 294–320. doi: 10.1016/j.icarus.2004.11.023

Hartmann, W. K., & Neukum, G. (2001). Cratering chronology and the evolution of Mars. *Space Science Reviews*, *96*(1/4), 165–194. doi: 10.1023/a:1011945222010

Howard, A. D. (2007). Simulating the development of Martian highland landscapes through the interaction of impact cratering, fluvial erosion, and variable hydrologic forcing. *Geomorphology*, *91*(3), 332–363. doi: 10.1016/j.geomorph.2007.04.017

Ivanov, B. A. (2001). Mars/moon cratering rate ratio estimates. *Space Science Reviews*, *96*(1/4), 87–104. doi: 10.1023/a:1011941121102

Kite, E. S., Lucas, A., & Fassett, C. I. (2013). Pacing early Mars river activity: Embedded craters in the aeolis dorsa region imply river activity spanned $\geq$(1–20)myr. *Icarus*, *225*(1), 850–855. doi: 10.1016/j.icarus.2013.03.029

Kite, E. S., Williams, J.-P., Lucas, A., & Aharonson, O. (2014, April). Low palaeopressure of the Martian atmosphere estimated from the size distribution of ancient craters. *Nature Geoscience*, *7*(5), 335–339. doi: 10.1038/ngeo2137

Lewis, K. W., & Aharonson, O. (2014, June). Occurrence and origin of rhythmic sedimentary rocks on Mars. *Journal of Geophysical Research: Planets*, *119*(6), 1432–1457. doi: 10.1002/2013je004404

Liang, M., Voller, V. R., & Paola, C. (2015a, January). A reduced-complexity model for river delta formation – Part 1: Modeling deltas with channel dynamics. *Earth Surface Dynamics*, *3*(1), 67–86. doi: 10.5194/esurf-3-67-2015

Melosh, H. J. (1989). *Impact cratering : a geologic process*. New York, NY: Oxford University Press.

Minton, D. A., Richardson, J. E., & Fassett, C. I. (2015). Re-examining the main asteroid belt as the primary source of ancient lunar craters. *Icarus*, *247*, 172–190. doi: 10.1016/j.icarus.2014.10.018

Richardson, J. E. (2009). Cratering saturation and equilibrium: A new model looks at an old problem. *Icarus*, *204*(2), 697–715. doi: 10.1016/j.icarus.2009.07.029

Russ, J. C. (1986). *Practical stereology*. Springer US. doi: 10.1007/978-1-4899-3533-5

Shannon, C. (1949). Communication in the Presence of Noise. *Proceedings of the IRE*, *37*(1), 10–21. doi: 10.1109/JRPROC.1949.232969

Smith, M. R., Gillespie, A. R., & Montgomery, D. R. (2008). Effect of obliteration on crater-count chronologies for Martian surfaces. *Geophysical Research Letters*, *35*(10). doi: 10.1029/2008GL033538

Warren, A. O., Kite, E. S., Williams, J.-P., & Horgan, B. (2019). Through the thick and thin: New constraints on Mars paleopressure history 3.8–4 ga from small exhumed craters. *Journal of Geophysical Research: Planets*, *124*(11), 2793–2818. doi: 10.1029/2019JE006178

Woronow, A. (1977). Crater saturation and equilibrium: A monte carlo simulation. *Journal of Geophysical Research (1896-1977)*, *82*(17), 2447–2456. doi: 10.1029/JB082i017p02447

Woronow, A. (1978). A general cratering-history model and its implications for the lunar highlands. *Icarus*, *34*(1), 76–88. doi: 10.1016/0019-1035(78)90127-6

Wright, K., Hariharan, J., Passalacqua, P., Salter, G., & Lamb, M. P. (2022). From grains to plastics: Modeling nourishment patterns and hydraulic sorting of fluvially transported materials in deltas. *Journal of Geophysical Research: Earth Surface*, *127*(11). doi: 10.1029/2022JF006769

Yielding, G., Needham, T., & Jones, H. (1996). Sampling of fault populations using subsurface data: a review. *Journal of Structural Geology*, *18*(2), 135–146. doi: 10.1016/S0191-8141(96)80039-3

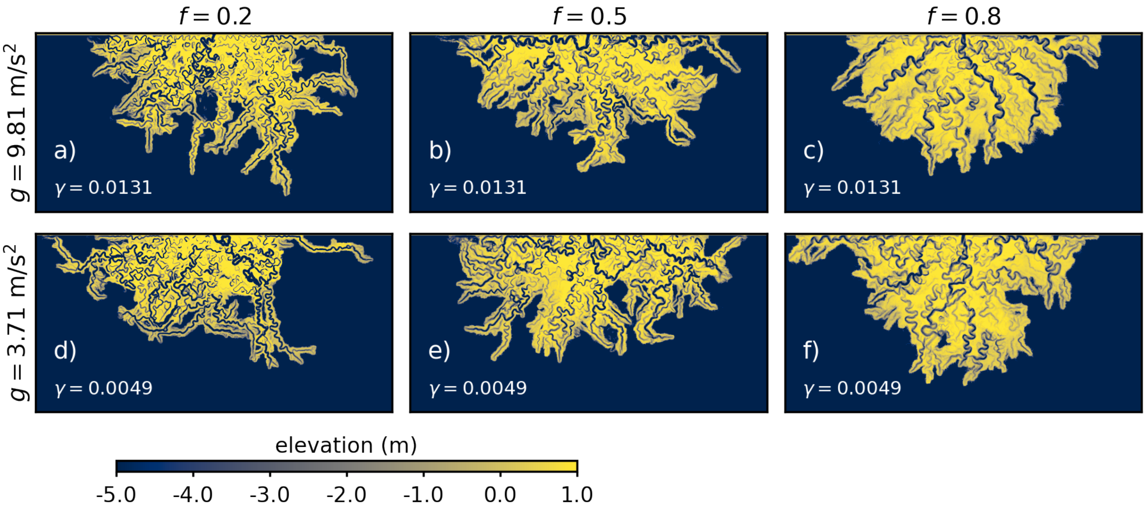

Figure S1. Simulation results examining the effect of gravity in the model. Varying gravity changes the parameter γ in the model. Qualitatively, this has very little effect on the delta deposit, and less of an impact than changing the input sand fraction. Importantly, these experiments are an incomplete representation of how gravity might affect delta growth on Mars; see text for full explanation.

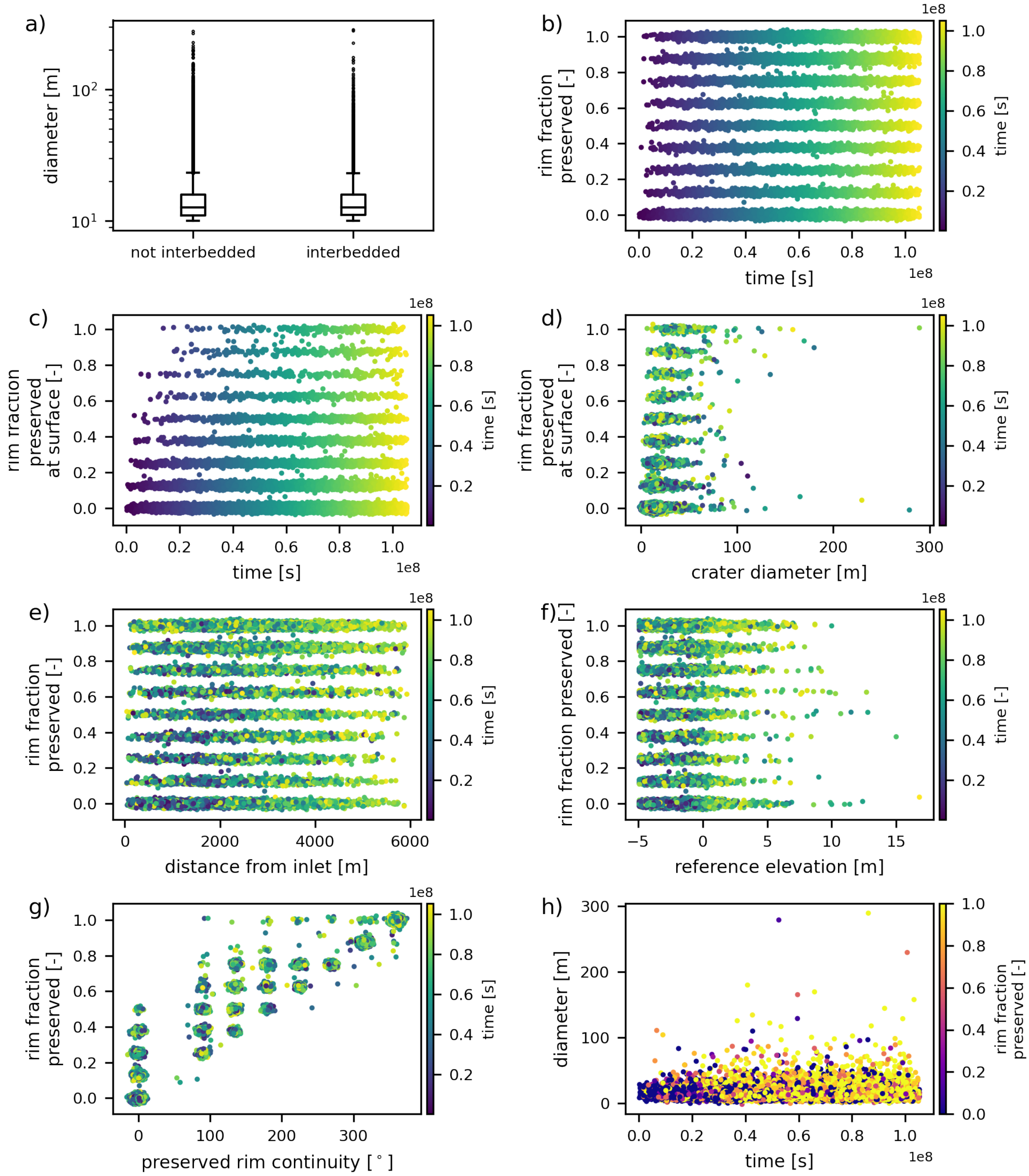

Figure S2. Additional assessments of crater preservation metrics. Overall, these analyses indicate that the delta model and crater analysis scripts are working as expected. See Section 2 for an interpretation of each panel.

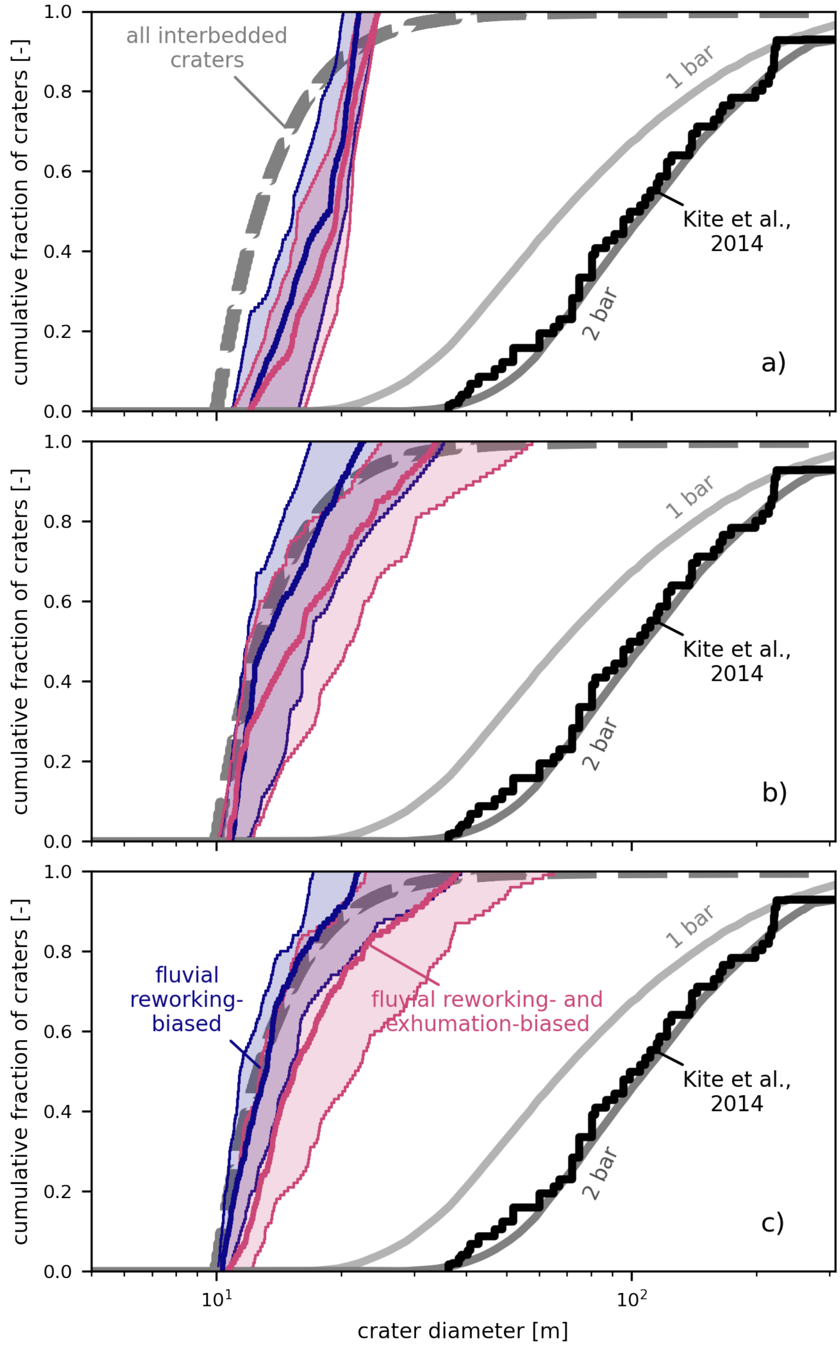

Figure S3. Cumulative distributions generated for a single simulation from the ensemble of each simulation duration, a) 1, b) 10, and c) 100 Myr. Only in the extreme case of fast deposition (1 Myr), it is possible to modify the distribution position, but even in this case, bias does not cause distribution to scale similarly to observed Mars interbedded crater record. Distributions were generated using only 11 crater samples (in contrast to 56 used in the main text) and repeated 100 times to assess distribution variability; figures show the median distribution as a solid line, and 16th to 84th percentile distribution as a shaded envelope.

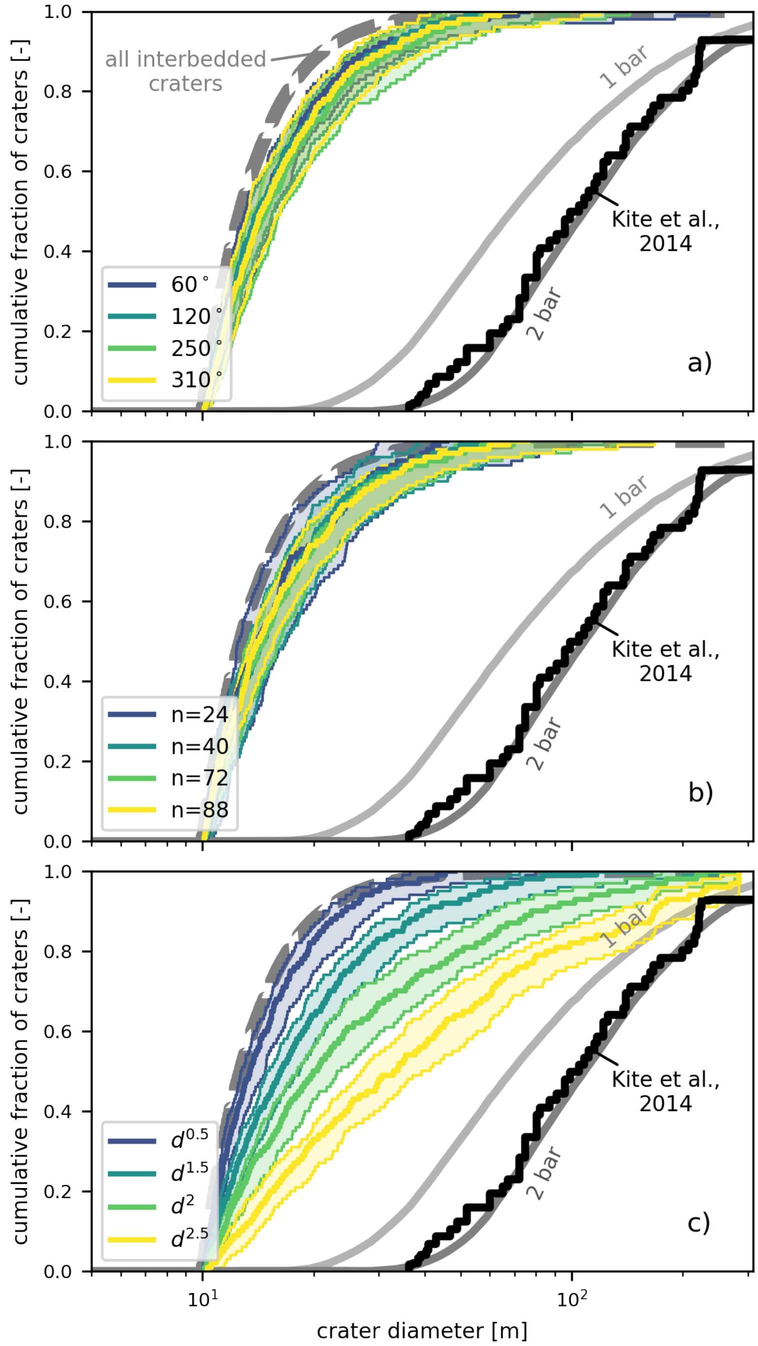

Figure S4. Cumulative crater size-frequency distributions generated for different parameter values used to threshold and modify data distributions in our workflow. a) Distributions generated for various rim continuity thresholds ranging from 60° to 310° (default is 180°, used throughout the main text). b) Distributions generated for various number of craters selected to include in the distribtuions ranging from 24 to 88 (default is 56, used throughout the main text). c) Distributions generated for various exhumation bia proportionalities with respect to crater diameter d, with proportionalities ranging 0.5 to 2.5 (default is 1, used throughout the main text).

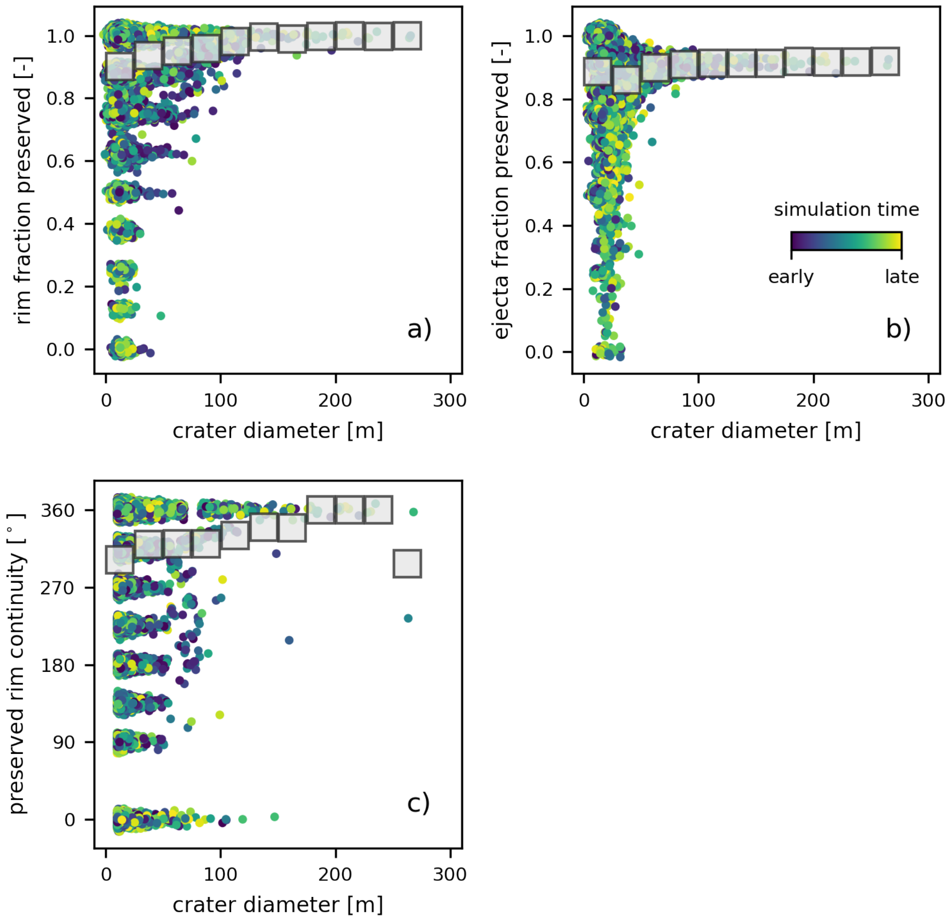

Figure S5. a) Rim fraction preserved, b) ejecta fraction preserved, and c) preserved rim continuity as a function of crater diameter for replicate simulations with no input sediment, to test crater obliteration by formation of new craters. Individual craters are colored by crater formation time within a simulation and have normally-distributed noise added for visualization to both axes (mean is 0, and standard deviation is ± 0.01 or $\pm 1.5°$, and ± 1.5 m), and gray boxes mark non-overlapping 25 m-bin averages. Smaller craters ($\lesssim$50 m) are obliterated more often than larger craters, which creates a smaller-crater bias in the crater record; notably, the magnitude of this bias is substantially reduced with respect to fluvial reworking bias (e.g., Figure 5).

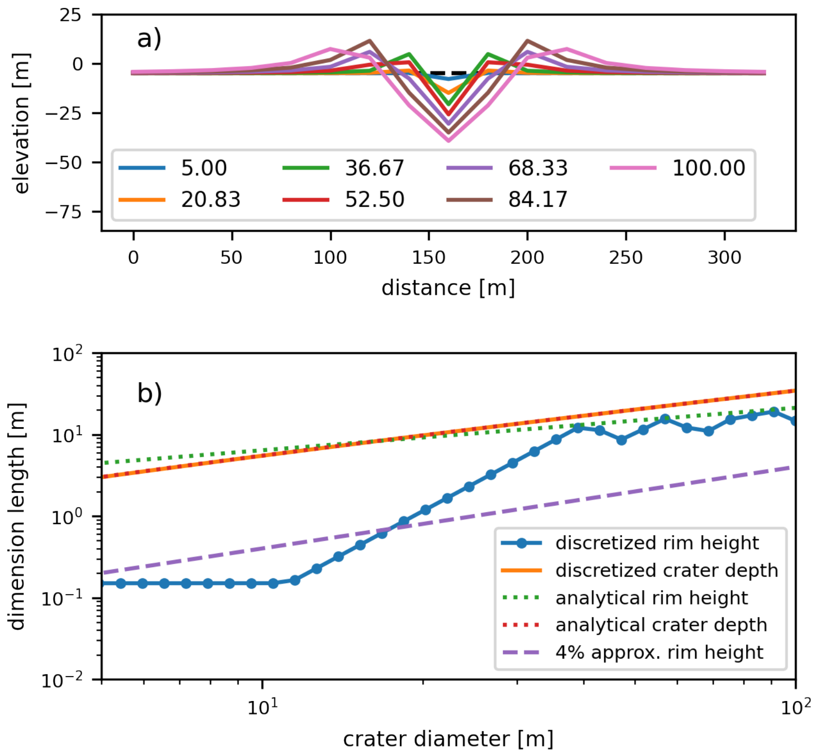

Figure S6. a) Topography of a transect through center of various diameter craters, as discretized to the model grid. b) Evaluation of crater discretized crater geometry compared to analytical geometry. Maximum crater rim height non-monotonically increases with increasing crater diameter. Discretized rim height is less than analytical rim height for modeled crater sizes $\lesssim 100$ m.

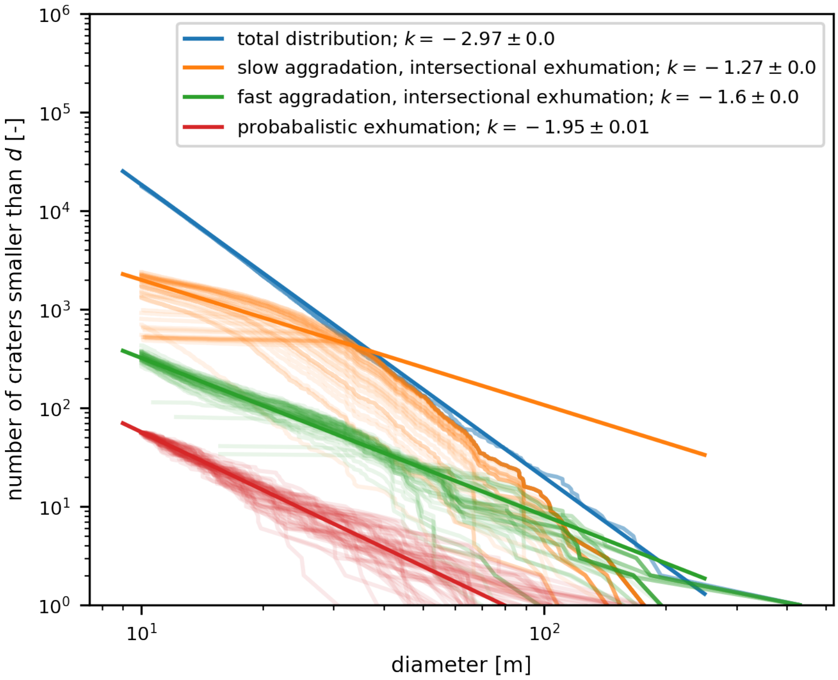

Figure S7. Crater size-frequency distributions generated from various empirical tests of potential exhumational bias. See text for more information.